

ADA 040247

RADC-TR-77-139
Final Technical Report
May 1977



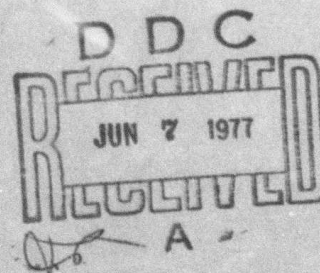
MULTIDITHER ADAPTIVE ALGORITHMS

Hughes Research Laboratories

Approved for public release; distribution unlimited.

Sponsored by
Defense Advanced Research Projects Agency (DoD)
ARPA Order No. 1279

The views and conclusions contained in this document are those of the authors and should not be interpreted as necessarily representing the official policies, either expressed or implied, of the Defense Advanced Research Projects Agency or the U. S. Government.



ROME AIR DEVELOPMENT CENTER
Air Force Systems Command
Griffiss Air Force Base, New York 13441

AU NO. _____
DDC FILE COPY

This report has been reviewed by the RADC Information Office (OI) and is releasable to the National Technical Information Service (NTIS). At NTIS it will be releasable to the general public, including foreign nations.

This report has been reviewed and is approved for publication.

APPROVED:

Robert F. Ogrodnik

ROBERT F. OGRODNIK
Project Engineer

Do not return this copy. Retain or destroy.

MULTIDITHER ADAPTIVE ALGORITHMS

R. C. Lind
M. L. Minden
S. Hansen
T. A. Nussmeier

Contractor: Hughes Research Laboratories
Contract Number: F30602-76-C-0022
Effective Date of Contract: 1 August 1975
Contract Expiration Date: 30 March 1977
Short Title of Work: Multidither Adaptive
Algorithms
Program Code Number: 6E20
Period of Work Covered: Aug 75 - Mar 77

Principal Investigator: Richard C. Lind
Phone: 213 456-6411
Project Engineer: Robert F. Ogrodnik
Phone: 315 330-4431

Approved for public release;
distribution unlimited.

This research was supported by the Defense Advanced Research Projects Agency of the Department of Defense and was monitored by Robert F. Ogrodnik (OCTM), Griffiss AFB NY 13441 under Contract F30602-76-C-0022.

UNCLASSIFIED

SECURITY CLASSIFICATION OF THIS PAGE (When Data Entered)

19 REPORT DOCUMENTATION PAGE		READ INSTRUCTIONS BEFORE COMPLETING FORM
1. REPORT NUMBER RADC-TR-77-139	2. GOVT ACCESSION NO.	3. RECIPIENT'S CATALOG NUMBER LC
4. TITLE (and Subtitle) MULTIDITHER ADAPTIVE ALGORITHMS,		5. REPORT NUMBER Final Technical Report, 1 Aug 75 - 30 Mar 77, N/A
6. AUTHOR(s) Richard C. Lind, T. A. Nussmeier M. L. Minden, S. Hansen		7. CONTRACT OR GRANT NUMBER(s) F30602-76-C-0022, DARPA Order-1279
8. PERFORMING ORGANIZATION NAME AND ADDRESS Hughes Research Laboratories 3011 Malibu Canyon Road Malibu CA 90265		9. PROGRAM ELEMENT, PROJECT, TASK AREA & WORK UNIT NUMBERS 62301E 16 1279 12790021 17000
10. CONTROLLING OFFICE NAME AND ADDRESS Defense Advanced Research Projects Agency 1400 Wilson Blvd Arlington VA 22209		11. REPORT DATE May 1977
12. MONITORING AGENCY NAME & ADDRESS (if different from Controlling Office) Rome Air Development Center (OCTM) Griffiss AFB NY 13441		13. NUMBER OF PAGES 75 12 80p.
		14. SECURITY CLASS. (of this report) UNCLASSIFIED
		15. DECLASSIFICATION/DOWNGRADING SCHEDULE N/A
16. DISTRIBUTION STATEMENT (of this Report) Approved for public release; distribution unlimited.		
17. DISTRIBUTION STATEMENT (of the abstract entered in Block 20, if different from Report) Same		
18. SUPPLEMENTARY NOTES RADC Project Engineer: Robert F. Ogrodnik (OCTM)		
19. KEY WORDS (Continue on reverse side if necessary and identify by block number) COAT Thermal Blooming Zernike Polynomial Deformable Mirror		
20. ABSTRACT (Continue on reverse side if necessary and identify by block number) Various analytic and experimental algorithms that can reduce the beam distortions caused by thermal blooming were investigated. A 19-element beryllium deformable mirror was used in the DARPA/RADC Coherent Optical Adaptive technique system to perform the experimental compensation studies. Using this system, both spatial and temporal algorithms employing zonal multidither and modal multidither using Zernike polynomials have been studied. A major result from this work is the identification of certain algorithms which can compensate for thermal blooming. The specific algorithms involved and the degree of correction.		

DD FORM 1 JAN 73 1473

EDITION OF 1 NOV 69 IS OBSOLETE

UNCLASSIFIED

SECURITY CLASSIFICATION OF THIS PAGE (When Data Entered)


172 600 M

UNCLASSIFIED

SECURITY CLASSIFICATION OF THIS PAGE(When Data Entered)

achieved depended on the blooming scenario studied. Experimental results indicated that the standard zonal system gave blooming correction over a larger set of parameters than did the Zernike polynomial system. This is believed to result from cross coupling and limited Zernikes - both caused by poor representation of the actual Zernike by the deformable mirror. Sequencing studies, both analytic and experimental, showed no preferred sequences but did indicate that focus and/or astigmatism always dominated the correction.

Numerical studies employing multidither coherent optical adaptive techniques, function maximization, and phase-conjugate algorithms were performed. Function maximization gave better correction than either of the other two. Servo convergence time was varied on the multidither system with the results indicating no change in correction.



UNCLASSIFIED

SECURITY CLASSIFICATION OF THIS PAGE(When Data Entered)

PREFACE

This report was prepared by Hughes Research Laboratories, Malibu, California, under contract F30602-76-C-0022. It is the final report on the contract and describes the analytic and experimental algorithm study for thermal blooming compensation using a deformable mirror multidither COAT system. The principal investigator and principal scientist is Dr. Richard C. Lind. The project is part of the adaptive optics program in the Opto-Electronics Department, managed by Dr. Viktor Evtuhov, at Hughes Research Laboratories.

FORM FOR	
White Section	<input checked="checked" type="checkbox"/>
Staff Section	<input type="checkbox"/>
INDEXED	<input type="checkbox"/>
SECTION	<input type="checkbox"/>
CLASSIFICATION/AVAILABILITY CODES	
FALL OUT OF SPECIAL	
A	

TABLE OF CONTENTS

Section	Page
PREFACE	3
LIST OF ILLUSTRATIONS	7
LIST OF TABLES	9
SUMMARY OF PROGRAM RESULTS	11
1. INTRODUCTION	13
A. Program Objectives	13
B. Research Program Plan	13
C. Report Organization	14
2. ANALYTIC BLOOMING COMPENSATION	15
A. Models	15
B. Servo Bandwidth Variation	25
C. Sequencing the Polynomial Channels	36
D. Conclusions	38
3. EXPERIMENTAL BLOOMING COMPENSATION	39
A. Experimental Setup	39
B. Algorithms	42
C. Scaling Considerations	43
D. Zonal COAT Performance	44
E. Modal COAT Performance	54
4. ZERNIKE-POLYNOMIAL/DEFORMABLE-MIRROR APPROXIMATION	61
A. Zernike Polynomials	61
B. Problem Definition	61

TABLE OF CONTENTS (Continued)

Section	Page
C. Selected Parameter Values	64
D. Computer Program	64
E. Output	66
5. RECOMMENDATIONS FOR FUTURE WORK	73
REFERENCES	75

LIST OF ILLUSTRATIONS

Figure		Page
1	Scaling the servo to the bandwidth f_g	22
2	Time-dependent correction — case I	26
3	Time-dependent correction — case II	27
4	Focal plane patterns — case II	30
5	Multidither predictive model — 1 channel	33
6	Multidither predictive model results — case II	34
7	Multidither Legendre sequencing — case I	37
8	Thermal blooming optical arrangement	40
9	Blooming cell	41
10	Intensity profiles	45
11	Photographs of bloomed beam	46
12	Peak target irradiance versus input power — zonal	47
13	Absolute Strehl ratio versus input power — zonal	49
14	Peak target irradiance versus input power — zonal	50
15	Peak target irradiance versus input power — zonal	51
16	Peak target irradiance versus input power — zonal	52
17	Peak target irradiance versus wind speed	53
18	Peak target irradiance versus input power — modal	56
19	Peak target irradiance versus input power — modal	57
20	Peak target irradiance versus input power — modal	58
21	Actuator array pattern	65
22	Tilt Zernike function	69
23	Focus Zernike function	70
24	Coma Zernike function	71

LIST OF TABLES

Table		Page
1	Propagation Parameters	25
2	Multidither-PPC Results	29
3	Nonlinear and Linear Results	35
4	Sample Case Results	36
5	Function Maximization Sequencing Results	37
6	Zernikes in DARPA/RADC System	54
7	Zernike Sequencing	59
8	Zernike Polynomials	62
9	Focus Zernike - 37 Actuators	68
10	Zernike Polynomial RMS Errors	72

SUMMARY OF PROGRAM RESULTS

The objective of this program on coherent optical adaptive techniques (COAT) is to investigate algorithms and techniques that can reduce the beam distortions caused by thermal blooming. This is the final report on the contract and describes the analytic and experimental work performed to determine algorithms that can compensate for thermal blooming. A description of the previous work on the contract can be found in Interim Reports 1, 2, and 3 (Ref. 1, 2, and 3).

A major result from the work conducted on this contract is the identification of certain multidither COAT algorithms employing a deformable mirror which can compensate for thermal blooming. The specific algorithms involved and the degree of correction achieved depend on the blooming scenario studied. Several spatial and temporal algorithms were studied both analytically and experimentally to determine their effectiveness for blooming compensation. In particular, under the analytic task, one-dimensional multidither COAT, function maximization, polynomial phase-conjugate algorithms, and initial transmitter irradiance profile algorithms have been numerically investigated. The results show that the function maximization algorithm yields the greatest correction with the phase conjugate and multidither COAT algorithms yielding somewhat poorer corrections. It was expected that the multidither algorithm would find a solution intermediate between the function-maximization and phase-conjugate solutions, approaching the nonlinear function-maximization solution as the servo convergence time was slowed. Instead, as the servo convergence time (inverse bandwidth) varied between practical limits of 0.04 and 20 msec, a linear (nearly phase-conjugate) solution was retained. We also found that the final converged multidither solution depended on the initial phase front of the mirror. Temporal sequencing of various polynomials (in this case, Legendre polynomials) did not improve the correction. However, sequencing did indicate that excellent correction could be achieved using only one particular polynomial.

PRECEDING PAGE BLANK NOT FILMED

Studies performed with various initial transmitter irradiance profiles indicate that the peak target irradiance can be maximized by making the aperture distribution as uniform as possible. This conclusion was found to hold for gaussian, truncated or apodized gaussian, annular or circular beams, and for special hole-in-the-middle laser modes. (See Ref. 1 and 2.)

Under the experimental task, zonal multidither and modal multidither employing Zernike polynomial algorithms were investigated. The zonal multidither achieved varying degrees of blooming correction over a wide range of scenario parameters. The modal system achieved correction for only one set of blooming parameters. We speculate that the modal results suffered because only lower-order Zernikes were used and because there was cross coupling among these Zernikes. This problem is the direct result of using only 19 actuators in the deformable mirror, which resulted in the mirror being a poor approximation to the actual analytic Zernike function. For the case where correction was achieved, a sequencing of Zernikes was performed. It was found that no improvement in correction was achieved for the various sequences performed consistent with the analytic results. In addition, it was found that only two Zernikes, focus and astigmatism, were needed to give the correction, again consistent with the analytic results.

Further algorithms employing auxiliary tracking and focus servos were also studied for blooming compensation. Results indicated tracking worked as expected, translating the wind-shifted bloomed beam to the bore-sight, while focus appeared to give no further correction over what the mirror alone would give.

As a preliminary to the use of the deformable mirror in the blooming studies, a characterization of the mirror was performed. A 37-element all-beryllium mirror was constructed; however, only 19 of the 37 elements were used because the supplier was unable to deliver all of the mirror actuators during the contract period.

Typical performance characteristics of the mirror were: actuator surface motion of $0.2 \mu\text{m}$ for 150 V drive; resonant frequencies existing in the 12 to 15, 18 to 20, and 24 kHz ranges; an influence function of $\exp(-5.396r^{1.71})$ for a faceplate thickness of 0.125 in.; and a mechanical coupling coefficient of 14%. Convergence times of 1.5 msec were obtained and tracking limits of 3 to 4 diffraction-limited beam diameters were measured. (See Ref. 3.)

SECTION 1

INTRODUCTION

A. PROGRAM OBJECTIVES

The primary objective of this program on coherent optical adaptive techniques (COAT) was to analyze and experimentally demonstrate adaptive multidither correction algorithms which can reduce beam distortions caused by thermal blooming. An additional program goal was to investigate the use of fixed transmitter intensity profiles to reduce thermal blooming.

B. RESEARCH PROGRAM PLAN

The research program used the DARPA/RADC experimental COAT system built and tested on contracts F30602-73-C-0248 and F30602-75-C-0001. Computer simulation codes developed on these contracts and on other programs (e. g., NSWC contract N60921-74-C-0249) were used for the analytical portions of this contract. These codes model the operation of several types of COAT servomechanisms and model the time-dependent propagation of optical beams in an absorbing and turbulent medium. The experimental investigations required constructing a deformable mirror for the COAT system. To accomplish the contract objectives, a research program consisting of four major tasks was developed. Task 1, an analytic task, consisted of computer simulation studies of blooming compensation algorithms. Task 2 was to design and construct a 37-actuator deformable mirror. In Task 3, the mirror was to be used to study thermal blooming compensation with zonal multidither control and with modal control using Zernike-polynomial modes. Task 4, an amendment to the contract, was to characterize the beryllium deformable mirror that was built and assess the applicability of the design to high-power laser COAT systems.

C. REPORT ORGANIZATION

This is the final report on this contract. The work reported previously in three interim reports¹⁻³ will not be repeated here, with the exception of the brief "Summary of Program Results" presented above. The interim reports dealt with Task 2 (deformable mirror construction), Task 4 (characterization of the mirror), and part of Task 1 (transmitter profile and initial Zernike blooming studies). The primary results from this contract which come from Task 1, analytic studies, and Task 3, experimental blooming compensation studies, are reported in this report. Section 2 discusses the analytic work performed on the computer to study various algorithms for blooming compensation. Section 3 describes the experimental program conducted for blooming compensation. Section 4 discusses the Zernike polynomial and how the deformable mirror was made to approximate the polynomials. Section 5 briefly discusses our recommendations for future work.

SECTION 2

ANALYTIC BLOOMING COMPENSATION

The goals of the analytic work on adaptive algorithms were to increase our understanding of and possibly to improve the dynamics of multidither response to thermal blooming. We hoped also to develop a model to predict the steady-state behavior of a multidither system.

To achieve these objectives, two areas were studied. First, we investigated the effect of varying the servo bandwidth. The motivation for this study resulted from the fact that the best correction for thermal blooming was invariably predicted by a nonlinear scheme which resembled infinitely slow multidither. The objective was to move toward this nonlinear correction by slowing the servo. Second, we analyzed temporal sequencing of the polynomial phase-correction channels to improve the blooming compensation. Polynomial multidither systems permit channel signal mixing when the phase distortions are large. Thus, simultaneous channel convergence of a system with initially large errors could easily find a nonoptimum correction path. Sequential channel convergence might yield path changes significant enough to find a different steady-state solution.

This section begins with an examination of the mathematical models used in this study, including the choice of a one-dimensional (1-D) propagation code, the linearities and nonlinearities of polynomial phase correction, and a discussion of computer codes which model the various optimization schemes. This is followed by the results of the bandwidth, sequencing, and predictive-modeling studies in one dimension and by the limited corroborative results in two dimensions.

A. MODELS

1. One-Dimensional versus Two-Dimensional Propagation Codes

Our studies used the first five Legendre polynomials to correct a simulated one-dimensional blooming medium. (Our nonlinear propagation codes proceed in ten steps from transmitter to focus. A one-dimensional code uses line rather than plane apertures at each propagation

step.) We chose a 1-D over a two-dimensional (2-D) code for the bulk of the work to allow more extensive runs: using a 2-D simulation to a steady state is prohibitively expensive. Using a 1-D approach has the disadvantage that a quantitative correspondence between the 1-D and 2-D simulations is lacking. From the results obtained, blooming compensation is better in 1-D than in 2-D. In addition, the Legendre polynomials have no exact analogs in Zernike polynomials. However, we believe that the qualitative results remain valid.

2. Polynomials

The first five Legendre polynomials and some associated Zernike functions are listed below. Note the difficulty in making simple analogs.

$P_n(x)$	$Z_{nm}(\rho, \theta)$
$P_1 = x$	$Z_{11} = \rho \cos \theta = x$
$P_2 = \frac{1}{2}(3x^2 - 1)$	$Z_{20} = 2\rho^2 - 1$
	$Z_{22} = \rho^2 \cos 2\theta = x^2 - y^2$
$P_3 = \frac{1}{2}(5x^3 - 3x)$	$Z_{31} = (3\rho^3 - 2\theta) \cos \theta$
	$Z_{33} = \rho^3 \cos 3\theta$ (1)
$P_4 = \frac{1}{8}(35x^4 - 30x^2 + 3)$	$Z_{40} = 6\rho^4 - 6\rho^2 + 1$
	$Z_{42} = (4\rho^4 - 3\rho^2) \cos 2\theta$
	$Z_{44} = \rho^4 \cos 4\theta$

$$P_5 = \frac{1}{8}(63x^5 - 70x^3 + 15x)$$

$$Z_{51} = (10\rho^5 - 12\rho^3 + 3\rho) \cos \theta$$

$$Z_{53} = (5\rho^5 - 4\rho^3) \cos 3\theta$$

$$Z_{55} = \rho^5 \cos 5\theta$$

3. Linear and Nonlinear Polynomial Response

Any system which deals with thermal blooming will be nonlinear. However, in this report we will consider a linear system to be one in which phase-correction measurements are made instantaneously: the medium has no time to respond to trial perturbations, and the system is optimized on a linearly propagated beam. A nonlinear response system is one in which optimization measurements on trial perturbations are made only under steady-state conditions.

The two may arrive at different solutions. Consider a mirror surface in the x plane focusing down to a point x_0 . The focal spot intensity is

$$I = U(x_0) U^*(x_0) , \quad (2)$$

where

$$U(x_0) = \int U(x) G(x, x_0) dx .$$

Expressing $U(x)$ in terms of amplitude and polynomial phase:

$$U(x) = u(x) e^{-jk \sum_n \beta_n P_n(x)} . \quad (3)$$

To maximize I with respect to a particular channel coefficient β_k requires

$$\frac{\partial I}{\partial \beta_k} = 0 = 2 \cdot \text{Re} \left\{ U^*(x_0) \frac{\partial U(x_0)}{\partial \beta_k} \right\}. \quad (4)$$

The last derivative determines linearity or nonlinearity. Since a linear system does not allow the medium to respond to the perturbation in β_k , it yields

$$\frac{\partial U(x_0)}{\partial \beta_k} = \int U(x) (-jkP_k(x)) (G(x, x_0)) dx. \quad (5)$$

A nonlinear system waits for the Green's function to respond, yielding

$$\frac{\partial U^*(x_0)}{\partial \beta_k} = \int U^*(x) \left[(+jkP_k(x)) G^*(x, x_0) + \frac{\partial G^*(x, x_0)}{\partial \beta_k} \right] dx. \quad (6)$$

Now, to find an expression for the correction signal, we make the following simplifications:

- Start with a uniform beam: $u(x) = 1$.
- Assume the Green's function has only a phase distribution, which depends on the phase-correction set $\beta = (\beta_1, \beta_2, \beta_3 \dots)$:

$$G(x, x_0) = \exp \left(-jk \sum_n a_n(\beta) P_n(x) \right). \quad (7)$$

This yields

$$\frac{\partial I}{\partial \beta_k} = 0 = 2 \cdot \operatorname{Re} \left\{ \int U(x) G(x) dx \int U^*(x) G^*(x) (jk) \left[P_k(x) + \sum_n P_n(x) \frac{\partial a_n(\vec{\beta})}{\partial \beta_n} \right] dx \right\}. \quad (8)$$

Further, assume that all net phase perturbations are small, i.e.,

$$\left| k(\beta_n + a_n(\vec{\beta})) < 1 \right|.$$

This allows linear expansion of the exponentials. Using the orthogonality of the polynomials, we find

$$\frac{\partial I}{\partial \beta_k} \approx -2 \left\{ \frac{(\beta_k + a_k(\vec{\beta}))}{g_k} + \sum_n \frac{(\beta_n + a_n(\vec{\beta}))}{g_n} \frac{\partial a_n(\vec{\beta})}{\partial \beta_k} \right\} = 0, \quad (9)$$

where g_n depends on the type of polynomial involved.

$$\text{Legendre: } g_n = \frac{(2n+1)}{2}$$

$$\text{Zernike: } g_n = (n+1), m=0 \quad (10)$$

$$g_n = 2(n+1), m \neq 0.$$

For a linear system the partial derivatives of Eq. (9) will be zero such that

$$\frac{\partial I}{\partial \beta_k} = 0$$

thus

$$\beta_k = -a_k(\vec{\beta}) \quad . \quad (11)$$

This is the phase-conjugate result. We will examine the nonlinear result in more detail later in this section to clarify some of the computer results.

4. Function Maximization and Polynomial Phase-Conjugate Models

Function maximization (FM) and polynomial phase conjugate (PPC) are two idealized systems which give corrections that lie at the extremes of nonlinearity and linearity. Function maximization finds the nonlinear solution. With each trial mirror deformation, a new steady-state medium is determined before glint intensity is calculated. One polynomial at a time is optimized, then held at its optimum while the next is varied. After one maximization cycle, all coefficients are varied simultaneously a few times, then the sample-and-hold sequencing starts again.

Phase conjugate is the simplest example of a linear correction system. Polynomial phase conjugate uses the return wave phase information of an ordinary phase-conjugate system and decomposes it into a sum of orthogonal polynomials. The new outgoing wavefront is then assembled from only those polynomials used in the multidither system being modeled.

5. Multidither Model

a. Nonlinear and Linear Multidither

Multidither (MD) systems exhibit a dynamic interplay between nonlinear and linear responses. Three time constants are involved:

τ_d = dither period

τ_m = time for medium to reach a steady state (outgoing beam held fixed)

τ_s = servo convergence time ($\equiv 1/\text{servo bandwidth } (f_s)$)
(also referred to as τ_c).

A slow system in which the medium can come to steady state after each dither "step" - ($\tau_d \geq \tau_m$) - should approach a nonlinear solution. A fast system ($\tau_s \ll \tau_m$) should approach a linear solution.

b. Constraints on the Servo Parameters

We have scaled the entire servo structure, including the dither frequencies, to the bandwidth f_s . This allows the interplay between τ_s and τ_m to be isolated as the only temporal variable. The servo scaling parameters are shown in Figure 1. Most values have been empirically determined.

c. Dither Period

A constraint exists which links τ_d to the servo bandwidth:

$$\left. \begin{array}{l} \Omega_o \geq 10 \cdot 2\pi f_s \\ \Delta\Omega \geq 4 \cdot 2\pi f_s \\ \tau_d \leq \frac{\pi}{\Omega_o + N\Delta\Omega} \end{array} \right\} \begin{array}{l} \text{empirical experimental} \\ \text{constraints} \\ \text{sampling theorem.} \end{array} \quad (12)$$

where

f_s = servo bandwidth

Ω_o = lowest dither frequency

$\Delta\Omega$ = distance between adjacent dithers

N = number channels .

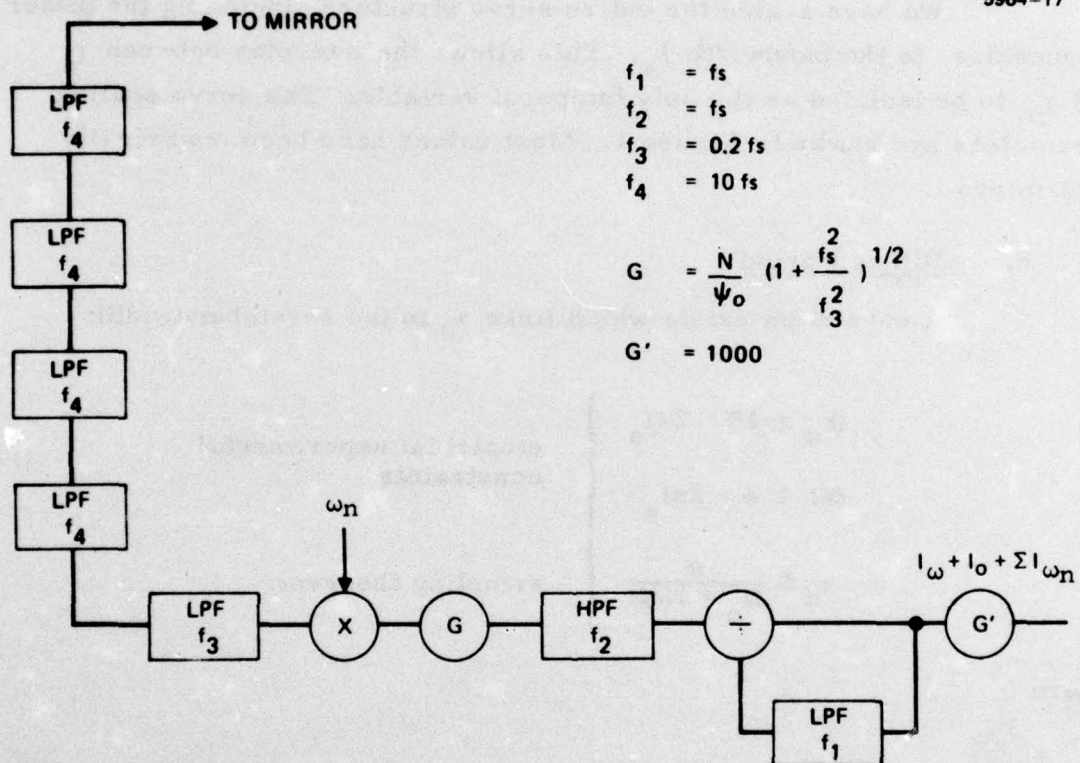


Figure 1. Scaling the servo to the bandwidth f_s .

d. Amplifier Gain

Each type of system (modal or zonal) requires a different calculation for the amplifier gain, G , so that it remains consistent with the desired servo bandwidth.

We need first to look at the open-loop gain g , of which G is a factor. The transfer function of the servo is dominated by a low-pass filter with a corner at f_o :

$$Z(f) = \frac{g}{(1 + if/f_o)} \quad (13)$$

Bandwidth f_s is defined as the point of unity gain:

$$|Z(f_s)| = 1$$

or

$$g = \left(1 + \frac{f_s^2}{f_o^2}\right)^{1/2} \quad (14)$$

Open-loop gain is given by

$$g = \frac{I_w}{I_o} \left(\frac{G}{2}\right), \quad (15)$$

where I_w/I_o is the signal at frequency w after the automatic gain control (AGC) and the factor 2 comes in after synchronous detection. In an N -channel zonal system, with a dither amplitude ψ_d on each channel,

$$\frac{I_w}{I_o} = 4 J_o(\psi_d) J_1(\psi_d) \left(\frac{1}{N} - \frac{1}{N^2}\right) \approx \frac{2\psi_d}{N}, \quad (16)$$

which gives

$$G \approx \frac{N}{\psi_d} \left(1 + \frac{f_s^2}{f_o^2} \right)^{1/2} . \quad (17)$$

In a polynomial system, the signal gain varies with the order of the polynomial,

$$\frac{I_w}{I_o} \approx \frac{2\psi_d}{g_n} , \quad (18)$$

where g_n was defined in Eq. (10) for both Legendre and Zernike polynomials. Uniform channel gain is ensured by defining a variable dither amplitude in each channel,

$$\psi_d(n) = \psi_o g_n .$$

This yields

$$G \approx \frac{1}{\psi_o} \left(1 + \frac{f_s^2}{f_o^2} \right)^{1/2} . \quad (19)$$

e. Medium Response to Dithers

The standard Hughes multidither code assumes a servo fast enough that the medium cannot respond to the dithers (i.e., a linear correction system). It does this by heating the medium only at discrete medium update times, with a beam phase averaged over the dither perturbations. In the intervals between update times, a Green's function is used to linearly propagate the dither beam. To see any nonlinearity in the correction, it is necessary to propagate the beam nonlinearity at each dither sample time, with an instantaneous rather than an averaged

phase profile. We implemented this as a code option: multidither with medium response (MDMR). This option led to expensive code run times; consequently, only a few runs were made.

B. SERVO BANDWIDTH VARIATION

1. Results

Multidither code results were expected to give a nonlinear solution with a slow servo, and a linear solution with a fast servo. However, as servo convergence time (inverse bandwidth) varied between practical limits of 0.04 and 20 msec, we retained a linear solution. From the same initial state, the system in all cases converged to the same position, or oscillated between the same limits. In addition, the 1-D correction was greater than that found in 2-D thermal blooming compensation.

Of the many cases studied, two are of primary interest (see Table 1 and Figures 2 and 3), both with uncorrected Strehl ratios around 0.5.

Table 1. Propagation Parameters

Case (I)	Case (II)
$\alpha = 2 \times 10^{-6}/\text{cm}$	$\alpha = 2 \times 10^{-6}/\text{cm}$
$P = 26 \text{ kW/cm}$	$P = 20 \text{ kW/cm}$
$v = 500 \text{ cm/sec}$	$v = 1275 \text{ cm/sec}$
$f = 2 \text{ km}$	$f = 2 \text{ km}$
$\Omega = 0.02 \text{ rad/sec}$	$\Omega = 0.005 \text{ rad/sec}$
$APO = 22 \text{ J/m}^3$	$APO = 17.3 \text{ J/m}^3$
$\rho_o = 70 \text{ cm}$	$\rho_o = 35 \text{ cm}$
$\rho_{1/e} = 53.5$	$\rho_{1/e} = 26.75$

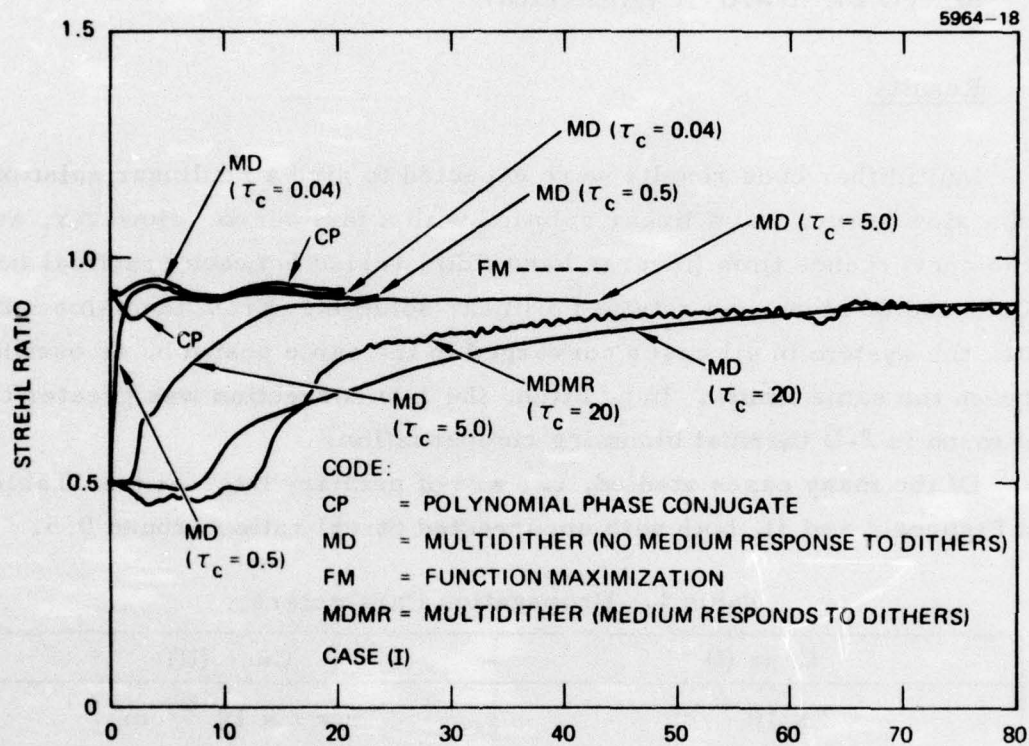


Figure 2. Time-dependent correction — case I.

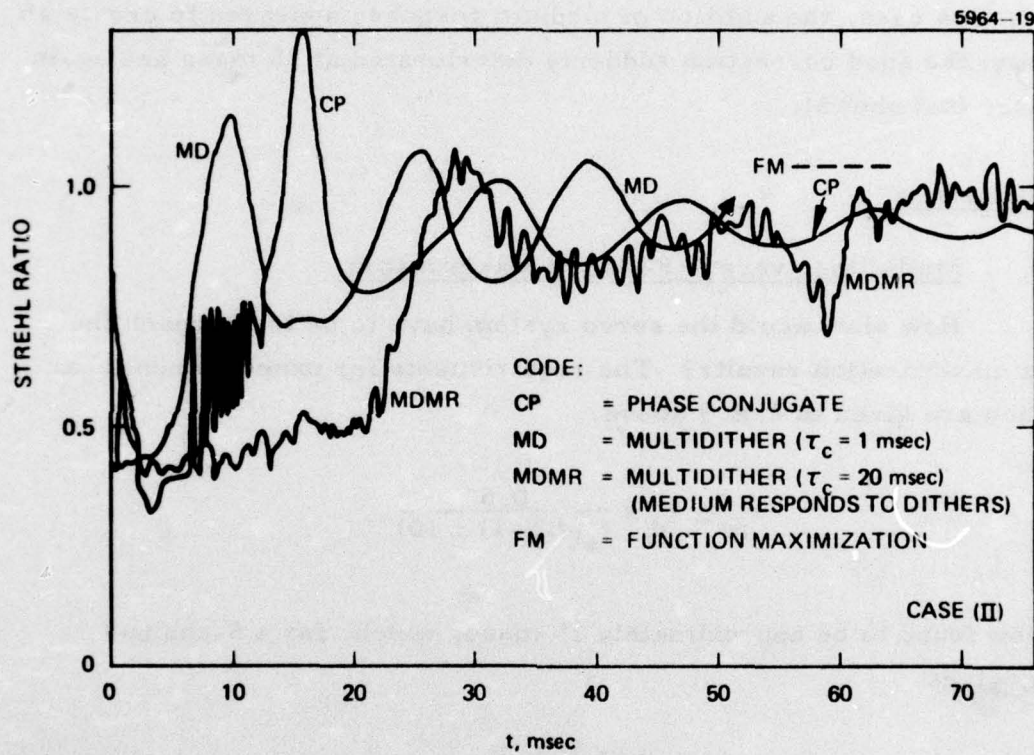


Figure 3. Time dependent correction — case II.

Case (I) converged steadily to a value of 0.9 for all servo convergence times. Even at $\tau_s = 20$ msec, and allowing the medium to respond to the dithers, no difference in Strehl ratio was observed.

Case (II) had less slewing than case (I). In the time allowed for the runs, peak intensity oscillated from 0.7 to over 1. The oscillation period was approximately 15 msec, the time it took the medium to reach a steady state. In this case, the addition of medium response appeared to create an instability; the good correction suddenly deteriorated at 58 msec and again at 85 msec (not shown).

2. Discussion

a. Multidither versus Function Maximization

How slow would the servo system have to be to approach the function maximization results? The requirements for expected nonlinear correction are given in 2.A.5 above.

$$\tau_m \lesssim \tau_d \leq \frac{0.5}{f_s(4(N-1) + 10)} \cdot$$

τ_m is now found to be approximately 15 msec, which, for a 5-channel system, gives

$$f_s \leq 1.3 \text{ Hz}$$

$$\tau_s \geq 0.8 \text{ sec}$$

This is too slow for any practical dither system.

b. Multidither versus Polynomial Phase Conjugate

Referring to Table 2, we see that multidither consistently found a somewhat poorer solution than did PPC when starting from a flat mirror. A better maximum was found when starting near the phase conjugate solution.

Table 2. Multidither-PPC Results

System (Case(I))	Target Intensity	Polynomial Solution				
		$P_1(x)$	$P_2(x)$	$P_3(x)$	$P_4(x)$	$P_5(x)$
Phase Conjugate	0.93	-7.5	-0.05	2.9	-0.53	-1.86
Multidither (No initial correction)	0.9	-9.8	0.1	0.02	-0.1	-3.54
Multidither (Starting at phase conjugate solution)	0.92	-7.8	0.08	3.4	-0.3	-2.15

The better solution using multidither can be understood with reference to Eqs. (8) and (9). Starting near the PPC coefficients results in smaller initial net phase distortions. Thus, the exponential linearization is more valid, complex interactions between propagating polynomials are of less importance, and the system is less likely to head for a secondary maximum. In our 1-D multidither, however, it appears that the secondary maximum is barely lower than the primary.

The PPC code gives instantaneous correction to the medium. The infinite bandwidth allows some initial instability in the correction for case II, which does not occur for multidither. However, the two settle down subsequently to almost identical temporal behavior.

As an interesting sidelight, we might speculate as to why the 1-D correction is so good. Figure 4 sketches the focal-plane patterns of the uncorrected and nonlinearly corrected beams of case II. For comparison, we have included the focal pattern of an unbloomed beam. For 2-D beam cross sections in general, it is unusual to see a bloomed beam which corrects to a Strehl ratio greater than 1, but not impossible. Wind probably causes the worst of the blooming to occur some distance back from the focus. If the beam reaches the end of the heated medium with a somewhat wider diameter than the unbloomed beam, it may focus down through the wind-cooled section with a smaller $f\#$ to a smaller focal spot. However,

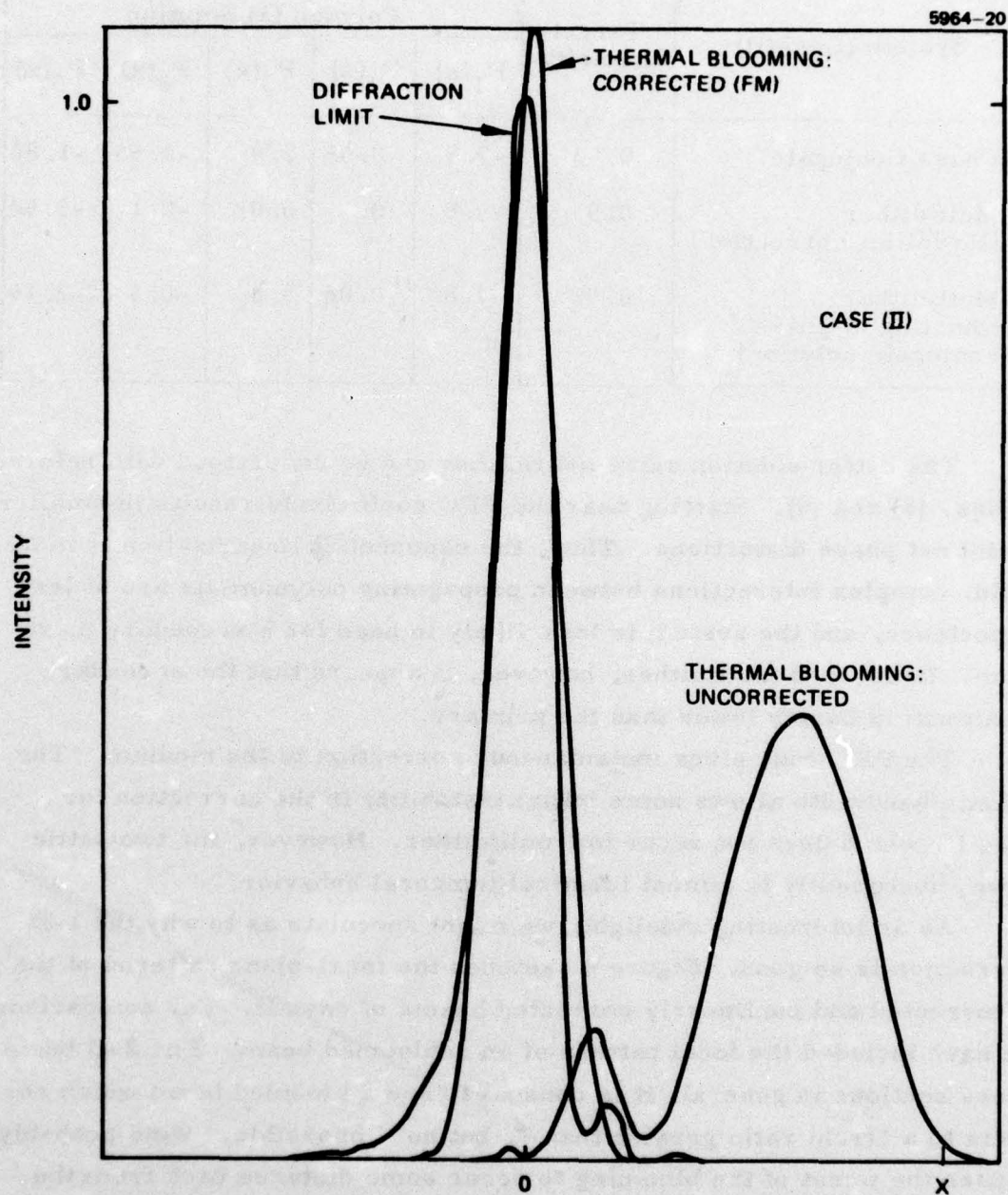


Figure 4. Focal plane patterns - case II.

since this description could be just as valid in 2-D as in 1-D, we are left with the same question: Why is 1-D correction so much better? Reexamination of Eq. (9), which delineates the linear and nonlinear portions of the correction, yields

$$\text{Linear: } \frac{\beta_k + a_k(\bar{\beta})}{g_k} = 0$$

$$\text{Nonlinear: } \frac{\beta_k + a_k(\bar{\beta})}{g_k} + \sum_{n=1}^N \frac{(\beta_n + a_n(\bar{\beta}))}{g_n} \frac{\partial a_n(\bar{\beta})}{\partial \beta_k} = 0 \quad (20)$$

Two points should be noted:

- This equation is derived from a treatment which assumed only phase distortions, and therefore has limited applicability to a real blooming situation.
- The N terms must include all polynomial coefficients which make a contribution to the phase description of the medium, even if many fewer correction channels are actually used.

It is easy to show that good steady-state correction is possible if the sum of the nonlinear terms of Eq. (20) is small compared to the linear term. In this case, the linear and nonlinear terms would lie close together.

In one-dimensional blooming, we have found the values of

$$\frac{\partial a_n(\bar{\beta})}{\partial \beta_k}$$

to be typically in the range from 0.01 to 0.05, yielding comparatively small nonlinear terms. Thus, one hypothesis on the superiority of the 1-D correction is that the polynomial interactions might be stronger in a 2-D than in a 1-D medium.

A second hypothesis is that the nonlinear terms are similarly small in one and two dimensions, but that the larger number of degrees of freedom increases the nonlinear correction contribution. If we were

to expand the list of Legendre and Zernike equivalents (Section 2.A.2), we would find that if a 1-D blooming medium required an N-polynomial description, a 2-D medium with comparable spatial frequencies would require approximately $(N^2 + 4N)/4$ terms.

c. Predicting the Steady-State Linear Solution

In a linear correction scheme, there are two opposing factors: linear correction drives the intensity to a peak, but medium response drives toward a steady state, usually diminishing the glint intensity. The simulations we ran seemed to indicate that, within limits, the relative time scales of the two processes are unimportant. This encouraged us to try a model in which the two were separated completely: a sequence of purely linear correction to some converged value, followed by the determination of a new steady-state medium. When the linear correction holds the system in the same state as the previous iteration, we can assume that a steady-state system solution has been reached.

Figure 5 shows how this works for one-channel tilt correction. The solid line gives target intensity at steady state as the transmitter tilts the focal pattern across the target. The maximum of this curve (at $\beta_1 = -19$, $I_0 = 0.43$) is the nonlinear solution. We start the predictive linear model at various initial tilt positions. The arrows indicate the direction of the system in converging to an instantaneous linear correction. The dashed lines give the change in intensity as the medium drives toward steady state. These sequences converge to a range of potential linear solutions about $\beta_1 = 16$, $I_0 = 0.39$. Only a few iterations were necessary to find this solution, which resulted in a huge saving of computer time.

This model was tested on the same cases used in the earlier multi-dither simulations:

- Case I: In very few iterations, the system converged to the same point as the earlier simulations.
- Case II: The system oscillated initially between the same limits seen in the full-scale simulations, then settled down to a good correction. This correction was then used as an initial condition in the full time-dependent simulation. The results, shown in Figure 6, indicate that the predictive model is valid.

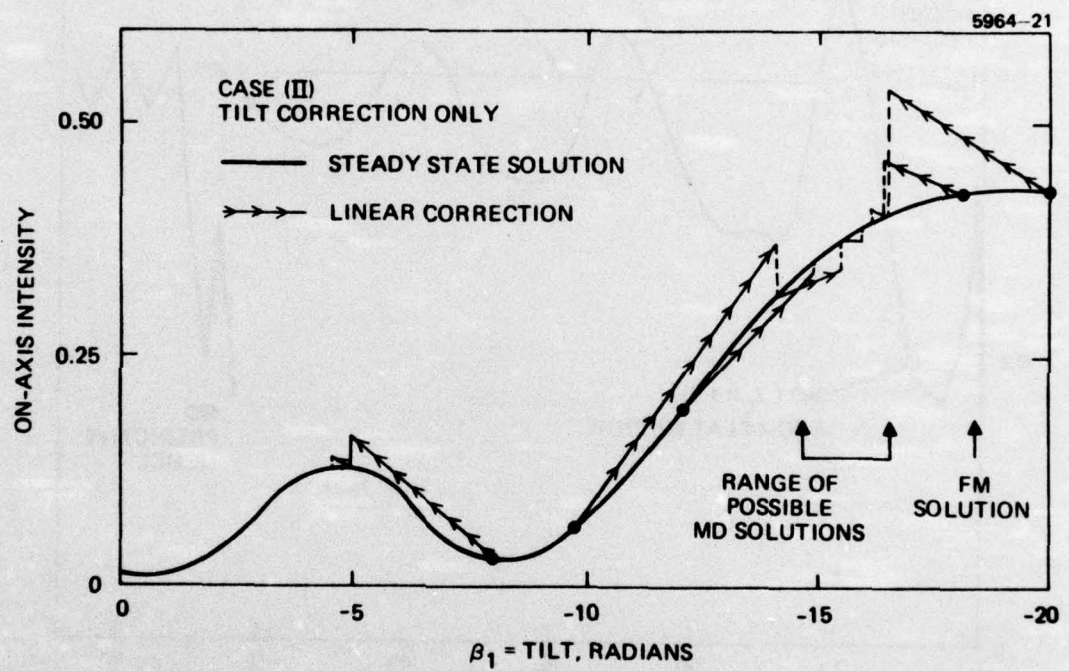


Figure 5. Multidither predictive model — one channel.

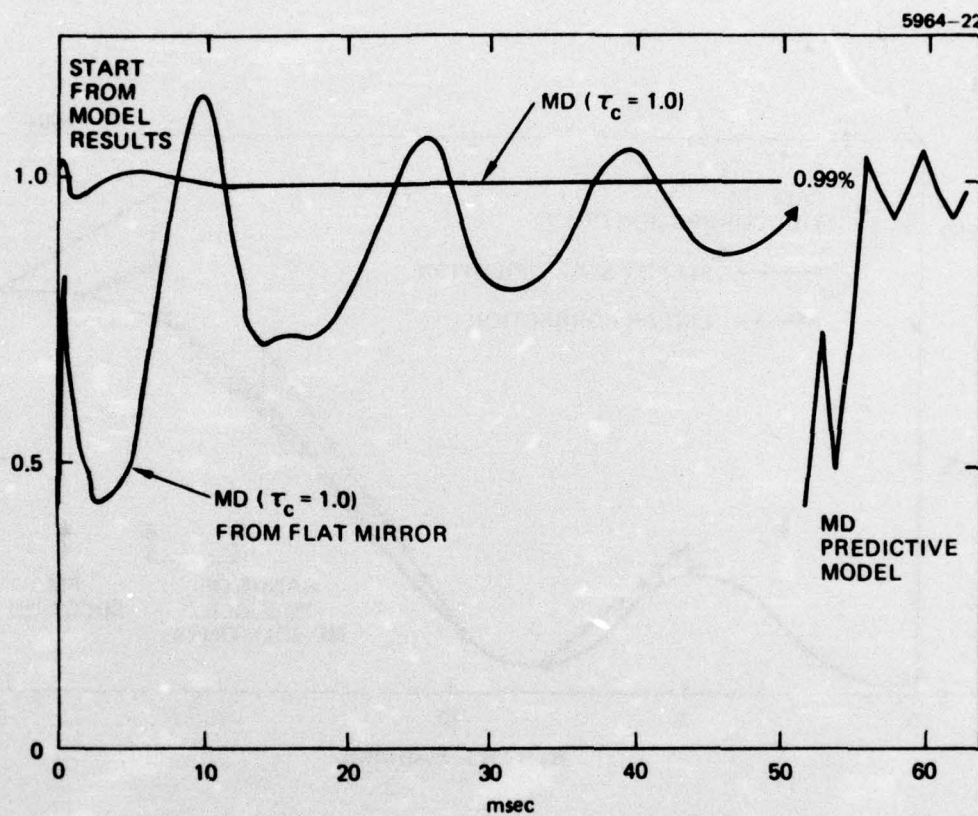


Figure 6. Multidither predictive model results — case II.

The nonlinear and linear solutions to Case II are presented in Table 3. We see that they are again very similar, as predicted.

Table 3. Nonlinear and Linear Results

Model	Steady-State Corrected Target Intensity	Polynomial Coefficients (radians)				
		P ₁	P ₂	P ₃	P ₄	P ₅
Nonlinear	1.05	-11	0.23	2.0	-1.8	-3.4
Linear prediction	0.98	-11	0.32	2.0	-1.1	-3.0
Multidither starting from linear prediction results	0.99	-10.7	0.26	2.2	-1.3	-2.8

Full-scale simulations in 2-D have been too expensive to permit their steady-state behavior to be investigated extensively. However, with the predictive linear model, this becomes feasible.

As indicated above, we might expect to see a greater discrepancy between the nonlinear and linear steady-state solutions in 2-D. We checked this for a sample case:

- Power = 375 kW
- Wind velocity = 12.5 m/sec
- Focal length = 2 km
- $\alpha = 2 \times 10^{-6}/\text{cm}$
- $\Omega = 0.02 \text{ radn/sec}$
- $\rho_0 = 35 \text{ cm}$
- $\rho_{1/e} = 26.75 \text{ cm}$

We obtained the following results:

Table 4. Sample Case Results

Model	On-Axis Intensity	Zernike Polynomial Coefficients (radians)						
		Z_{11}	Z_{20}	Z_{40}	Z_{31}	Z_{22}	Z_{33}	Z_{42}
Nonlinear	0.42	4.0	-0.25	-0.12	-1.5	1.6	1.2	-0.12
Linear prediction	0.33	4.7	-0.98	0.01	-1.4	2.8	1.5	-0.87

The discrepancies are indeed greater and the correction not as good as in 1-D.

C. SEQUENCING THE POLYNOMIAL CHANNELS

1. Multidither

We investigated whether changing the polynomial sequences would create a maximization path from an initially flat mirror to a better solution.

Figure 7 shows the results of three of the five cases which were run. The arrows indicate the time at which a subsequent channel was added, and the numbers give the order of the added polynomial. In all cases, the tilt correction was the first to be stabilized.

In every case, the sequencing system converged to the same secondary solution found by the simultaneous channel multidither system. In this solution, $P_5(x)$ is so strongly dominant that no significant correction is seen until its channel is cut in.

2. Function Maximization

Our FM code does a form of sequencing as it varies one polynomial coefficient at a time. We changed the sequence of the polynomials and found that the path could be shifted from one maximum to another, as shown in Table 5 for case I (the FM system).

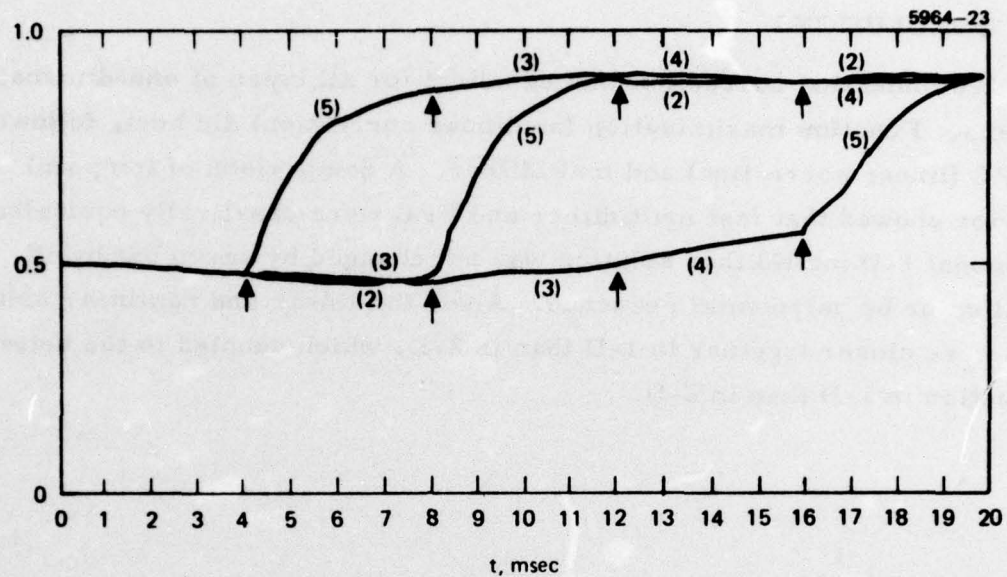


Figure 7. Multidither Legendre sequencing - case I.

Table 5. Function Maximization Sequencing Results

Polynomial Sequence	Intensity	Polynomial Coefficients			
		P_2	P_3	P_4	P_5
3 - 5 - 2 - 4	0.895	0.095	6.97	-0.1	-0.5
2 - 3 - 4 - 5					
5 - 3 - 4 - 2	0.97	-0.04	0.68	-0.22	-3.85
4 - 2 - 5 - 3					
2 - 4 - 3 - 5					

We do not know whether this is caused by the nonlinearity of the FM solution or by the freezing of previously maximized coefficients. The multidither sequencing code permitted previous channels to continue optimizing as new ones were added.

D. CONCLUSIONS

We found that correction was excellent for all types of one-dimensional systems. Function maximization (nonlinear correction) did best, followed by PPC (linear correction) and multidither. A comparison of temporal behavior showed that fast multidither and PPC were practically equivalent. The modal 1-D multidither solution was not changed by servo bandwidth variation or by polynomial sequence. Also, the linear and nonlinear solutions were closer together in 1-D than in 2-D, which coupled to the better correction in 1-D than in 2-D.

SECTION 3

EXPERIMENTAL BLOOMING COMPENSATION

This section presents a detailed discussion of the experimental measurements related to thermal blooming compensation which were made during this contract. Various algorithms are described, a 19-actuator zonal compensation algorithm, a modal algorithm employing Zernike polynomials, and in addition, the use of an auxiliary focus and tracking servo is discussed.

A. EXPERIMENTAL SETUP

The experimental measurements were made on the DARPA/RADC COAT system modified to incorporate the deformable mirror and the necessary electronics for the Zernike polynomial studies. A detailed description of these modifications is given in interim reports 2 and 3 and will not be repeated here.^{2,3}

The optical arrangement used in making these measurements is shown in Figure 8. There are two optical paths, one known as the "local loop," which is an undistorted path, and a propagation path where the blooming distortions are introduced. In these experiments, a liquid absorption cell was used to simulate the scaled thermal blooming conditions encountered by focused beams propagating over relatively short, low-altitude paths in the atmosphere. This cell was previously used on contract F30602-75-C-0001 and is discussed in the final report⁴ on that contract. The cell (shown in Figure 9) is 20 cm long with flow transverse to the length dimension. Methanol, with a small amount of iodine added to absorb the 0.488 μm laser light, was the liquid used.

In a blooming experimental sequence photomultiplier (PMT) 1 is connected to the COAT servo system and a near diffraction-limited beam is produced in the local loop at target plane 1. In addition, this beam is put into the propagation path containing the auxiliary tracking and focus controls and the liquid blooming cell. The peak target irradiance (or equivalently the Strehl ratio) at target plane 2 is then measured. This gives the NO COAT

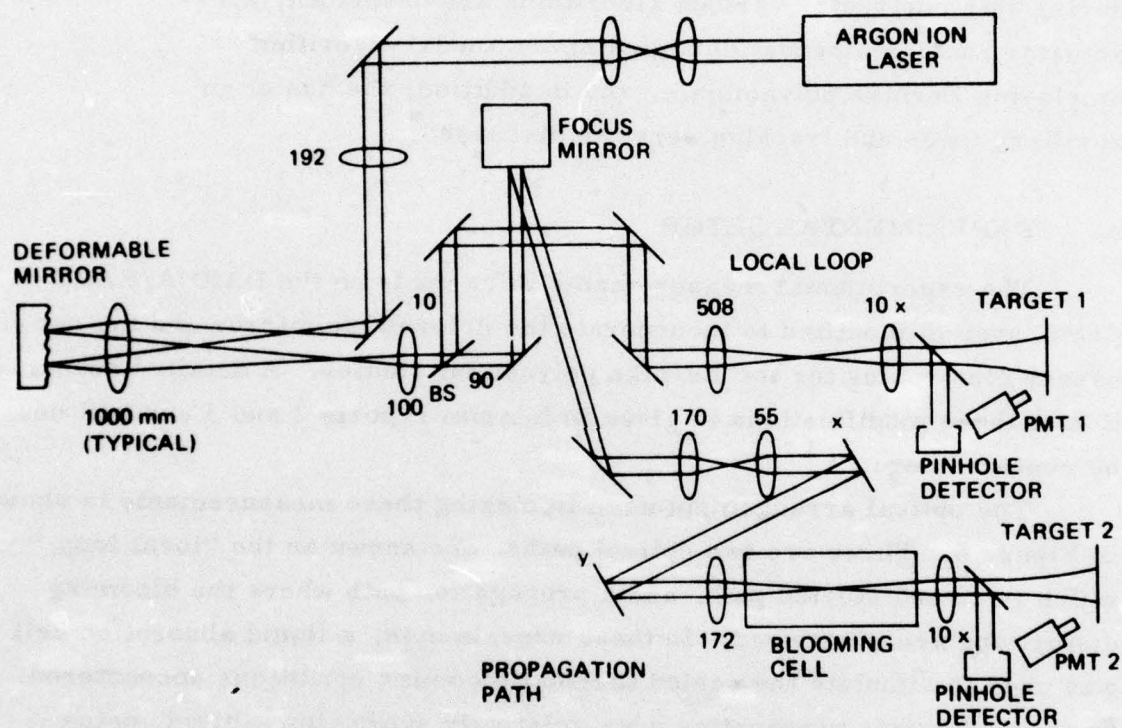


Figure 8. Thermal blooming optical arrangement.

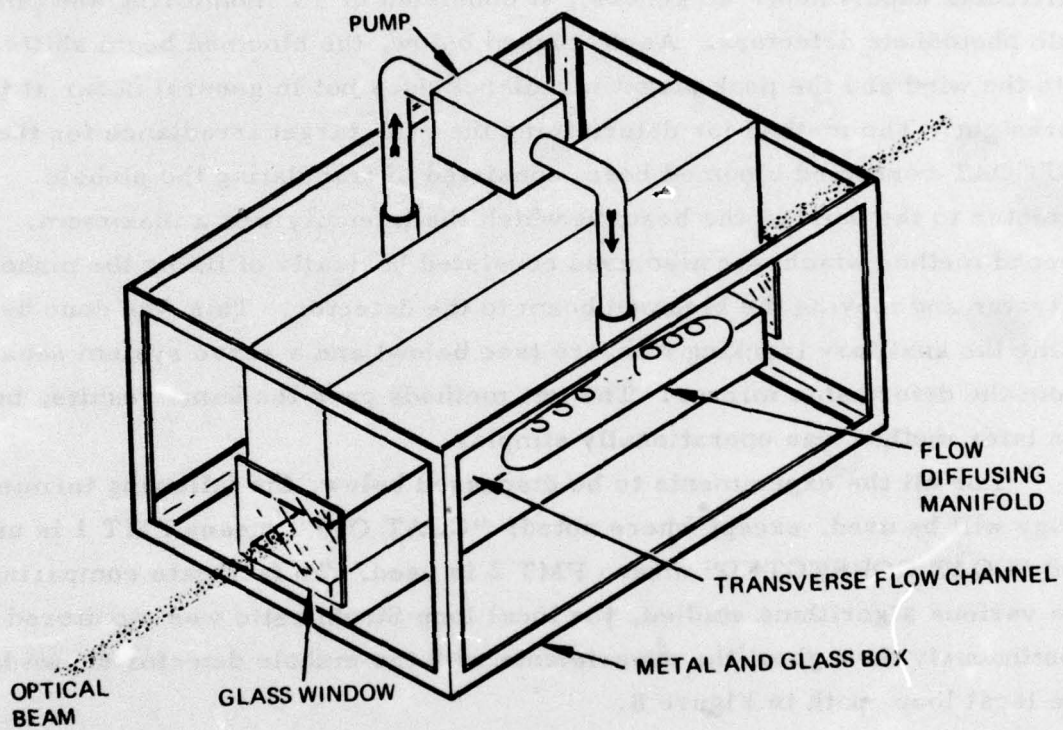


Figure 9. Blooming cell.

corrected Strehl ratio of the bloomed beam. When PMT 2 is subsequently connected to the COAT servo system, the degree of COAT correction of the bloomed beam is determined.

The diagnostics used to analyze system performance depended on the particular experiment. In general, it consisted of TV monitoring and pinhole photodiode detectors. As discussed below, the bloomed beam shifts into the wind and the peak target irradiance does not in general occur at the boresight. The method for determining the peak target irradiance for the NO COAT corrected bloomed beam consisted of translating the pinhole detector to the point in the beam at which the intensity was a maximum. A second method which was also used consisted basically of fixing the pinhole detector and moving the bloomed beam to the detector. This was done by using the auxiliary tracking mirrors (see below) and a servo system separate from the deformable mirror. The two methods gave the same results, but the later method was operationally simpler.

For all the experiments to be discussed below, the following terminology will be used, except where noted: "COAT OFF" means PMT 1 is used and "COAT CORRECTED" means PMT 2 is used. To facilitate comparing the various algorithms studied, the local loop Strehl ratio was monitored continuously throughout the experiments with the pinhole detector shown in the local loop path in Figure 8.

B. ALGORITHMS

Within the limitations of the experimental equipment, various temporal and spatial algorithms were investigated to determine their degree of compensation for thermal blooming. Included for spatial algorithms were a 19-actuator deformable mirror zonal mode and a 5-Zernike polynomial modal mode. For temporal algorithms, sequencing of the 5 Zernikes was included. In addition, the auxiliary tracking and focus controls were studied with various combinations of the above algorithms. The tracking and focus servos have dither frequencies of 1 kHz and 100 Hz, respectively. It was hoped that these slower dithers would represent a temporal algorithm different from the deformable mirror system at the higher dither frequencies (~10 to 30 kHz). Consequently, track and focus represent both a temporal

and a spatial algorithm. From the analytic results (see Section 2), it appears that dither frequencies much lower than 100 Hz are required before a temporal effect on blooming compensation can be observed. This is consistent with the observed experimental results (see below).

C. SCALING CONSIDERATIONS

The laboratory experiments performed on this contract are scaled so that the results can be extended to other wavelengths, ranges, etc. In particular, our visible wavelength experiments are chosen to scale to a typical 10.6 μm scenario.

According to Bradley and Herrmann,⁵ the propagation of a slewed beam through an absorbing medium can be characterized by four dimensionless parameters:

- Absorption number $N_A \equiv \alpha R$
- Fresnel number $N_F = Ka^2/R$
- Slewing number $N_\omega = \omega R/v$
- Distortion number $N_D = -\frac{4\pi n_T \alpha R P}{n \rho C_P v a \lambda}$,

where α is the absorption coefficient, R is the range, K is the wave-number, a is the $1/e$ radius at the cell entrance, ω is the slewing frequency, v is the cross-wind velocity, n_T is the coefficient of index change with respect to temperature, n is the index of refraction, P is incident laser power, ρ is medium density, C_P is specific heat at constant pressure of the medium, and λ is wavelength of the laser. In addition, for typical 10.6 μm thermal blooming scenarios, heat transfer in the beam is convection rather than conduction dominated. Hence, for laboratory experiments, the wind speed and beam size must be chosen to ensure a convection-dominated situation. This can be satisfied by requiring that the Peclet number be much greater than one. The Peclet number, which is the ratio of convection to conduction, is given by

$$P_e = \frac{2va}{k/\rho C_P} ,$$

where K is the medium thermal conductivity. For the present experiments, $P_e \sim 50$; hence, convection dominates, the distortion number varies from 0.6 to 60, the Fresnel number is typically 130, the absorption number is ~ 0.2 , and there is no slewing.

Although these parameters characterize the blooming medium, it is crucial to know the relationship of the focused beam path to the length of the blooming cell and to the position of the blooming cell in the beam path. In previous studies,⁴ the effect of near-field or far-field blooming was presented, illustrating this importance. In the present laboratory experiments, the entire focused beam path is within the blooming medium as it would be in a scaled scenario.

D. ZONAL COAT PERFORMANCE

A typical intensity profile for both a local loop beam and a bloomed beam with a high distortion number ($N_D \sim 20$) is shown in Figure 10. Qualitative comparisons in amplitude should only be inferred because the TV camera used to generate this data is nonlinear. This data is actually taken with the Zernike mode, but in fact the data in the 19 actuator zonal mode is essentially the same.

Figure 11 gives a sequence of COAT OFF and COAT CORRECTED photographs of the beam profile taken for three distortion numbers, from a condition of essentially no blooming to a case of strong blooming (the $f\#$ of the TV camera is shown). We see the expected crescent-shaped beam for the strong blooming case. Further, the beam was shifted into the wind, as expected (not shown). Figure 12 shows the peak target irradiance as a function of input power for the data of Figure 11. These results are for $N_A = 0.2$, $N_D = 318$ P, and $N_F = 134$. Plotted are results for COAT OFF, COAT CORRECTED, and for no blooming (linear with power). The COAT system increases the peak target irradiance by up to a factor of 1.8 at a power input of ~ 20 mW. But as the power is further increased, correction decreases until virtually no correction is achieved at the higher powers. However, we can see from Figure 11 that, at the high power condition, there is a correction obtained which, although it would not affect the peak target irradiance, would result in a higher irradiance if a larger aperture were used.

INTENSITY
(BEAM INTENSITY 5 x LESS
THAN BLOOMED PATH BEAM)

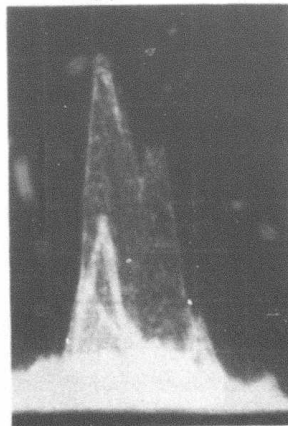
LOCAL LOOP
COAT-ON



(a)

INTENSITY

BLOOMED PATH
NO COAT CORRECTION
P = 56 mW



(b)

Figure 10. Intensity profiles.

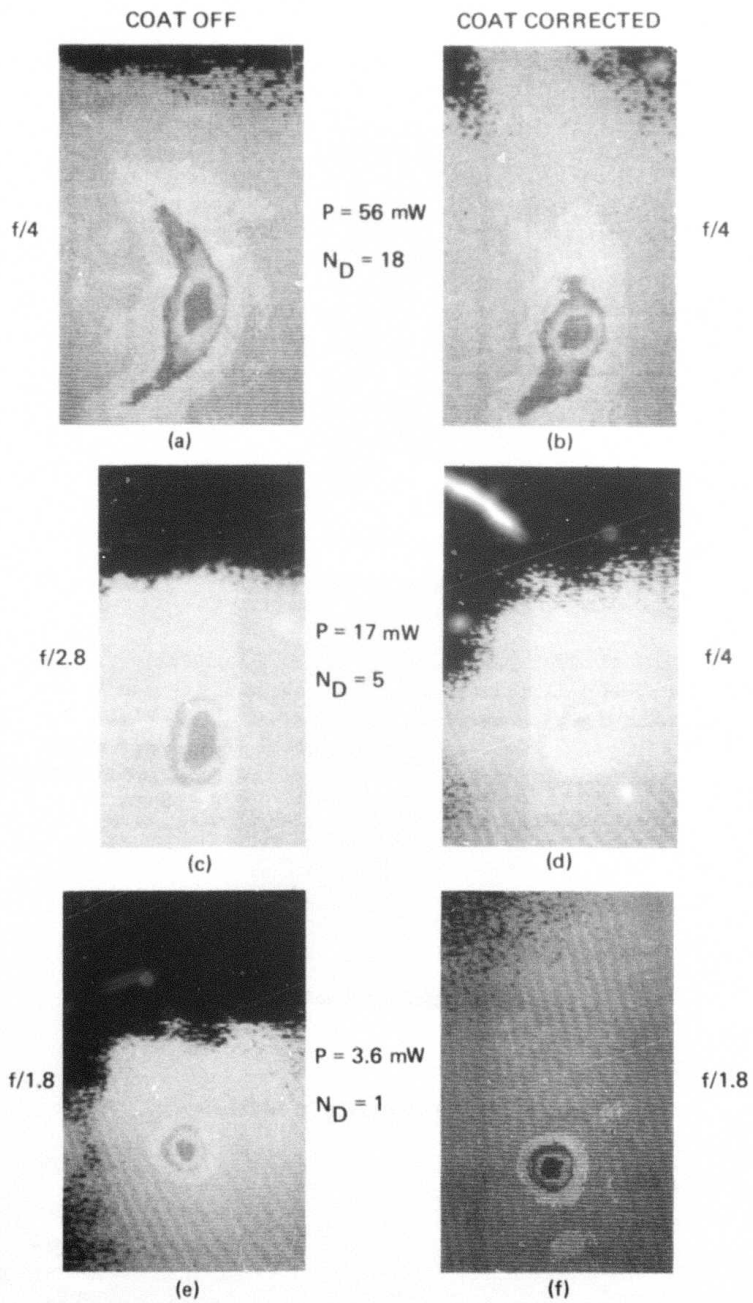


Figure 11. Photographs of bloomed beam.

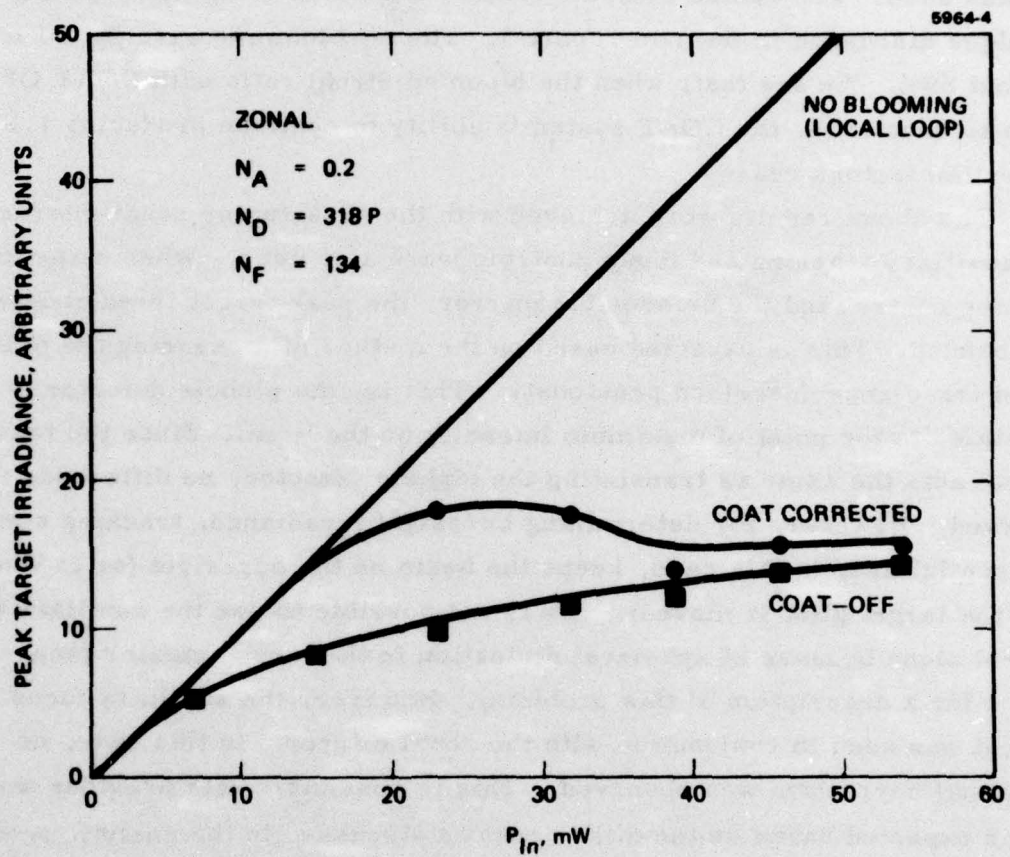


Figure 12. Peak target irradiance versus input power — zonal
 $N_A = 0.2$, $N_D = 318P$, $N_F = 134$.

Absolute Strehl ratio was determined for this case and the results are shown in Figure 13. In determining the Strehl ratio, a truncated gaussian near-field input beam profile of measured truncation radius and $1/e^2$ intensity was used. The radius measurements were made using the scanning technique discussed in interim report 3. The no-blooming case Strehl ratio is about 80%. We see that, when the bloomed Strehl ratio with COAT OFF drops to about 30%, the COAT system's ability to continue producing 1.8 correction factors ceases.

The above results were achieved with the 19-actuator zonal mirror. The auxiliary tracking and focus controls were also used. When using the tracking control and the deformable mirror, the peak target irradiance was not changed. This is expected based on the method of measuring the peak target irradiance described previously. That is, the pinhole detector is translated to the point of maximum intensity on the beam. Since the tracking control acts the same as translating the pinhole detector, no difference is observed. However, for determining boresight irradiance, tracking control is essential and, in this case, keeps the beam on the boresight (or to wherever the target glint is moved). It was not possible to use the auxiliary focus control alone because of spherical distortion in the focus actuator (see Ref. 4 for a description of this problem). However, the auxiliary focus control was used in conjunction with the zonal mirror. In this case, no additional correction was observed. This is consistent with previous work⁴ and is expected based on the dither results discussed in the analytic section (Section 2).

Figures 14, 15, and 16 give similar plots of peak target irradiance as a function of input power for three sets of the parameters N_A , N_D , and N_F . Correction was achieved in all cases. Of the three parameters, it appears that the Fresnel number is the most critical in establishing the level of blooming and the level of COAT correction, with the best correction achieved for the cases with large Fresnel numbers. For these cases, operation with the auxiliary focus and tracking controls was also performed with results consistent with those discussed above.

One test was performed with input power fixed but wind speed variable. The results of this test are shown in Figure 17, which gives peak target

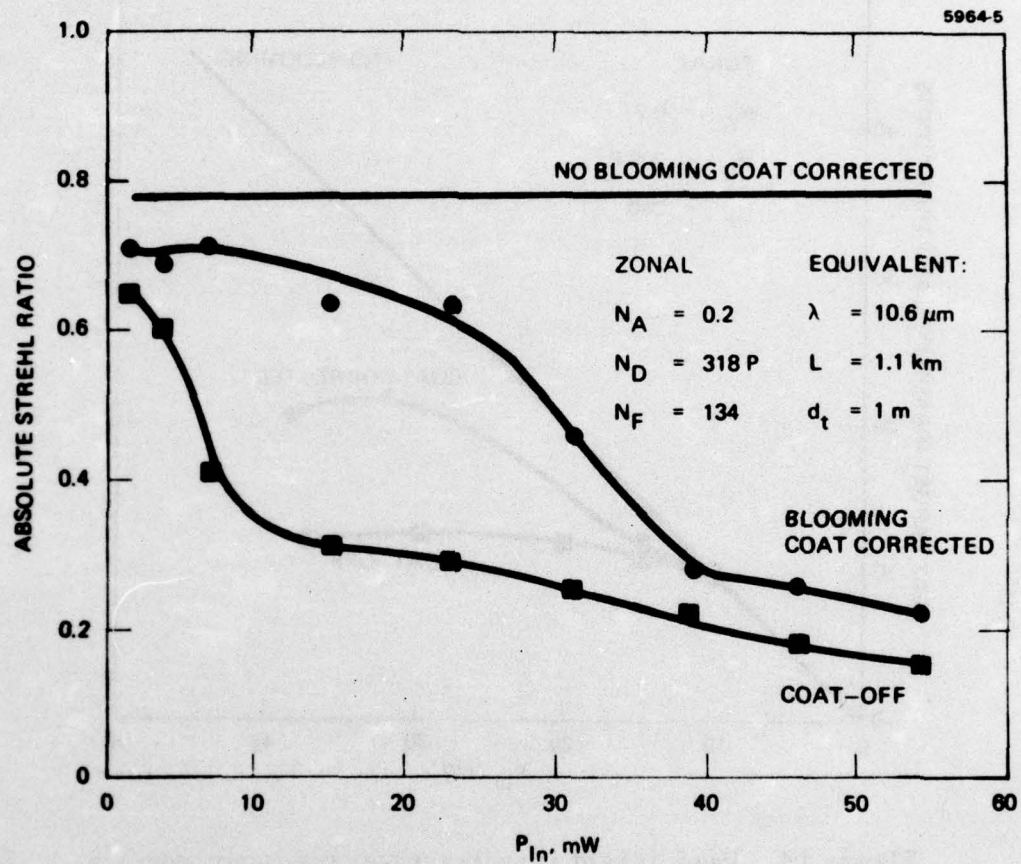


Figure 13. Absolute Strehl ratio versus input power — zonal.

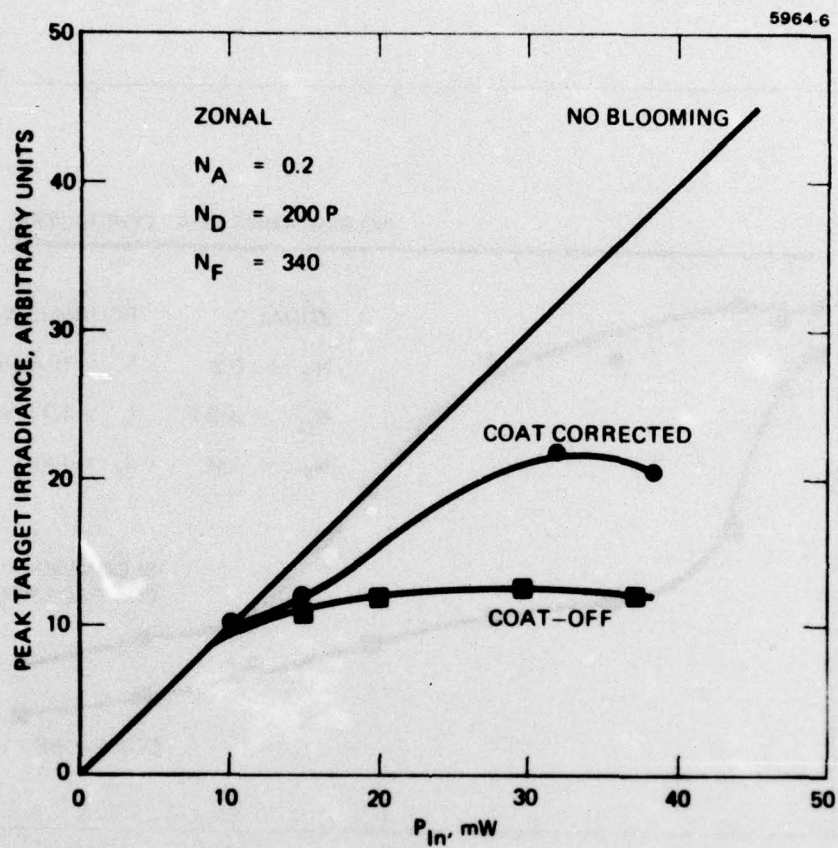


Figure 14. Peak target irradiance versus input power—zonal. $N_A = 0.2$, $N_D = 200P$, $N_F = 340$.

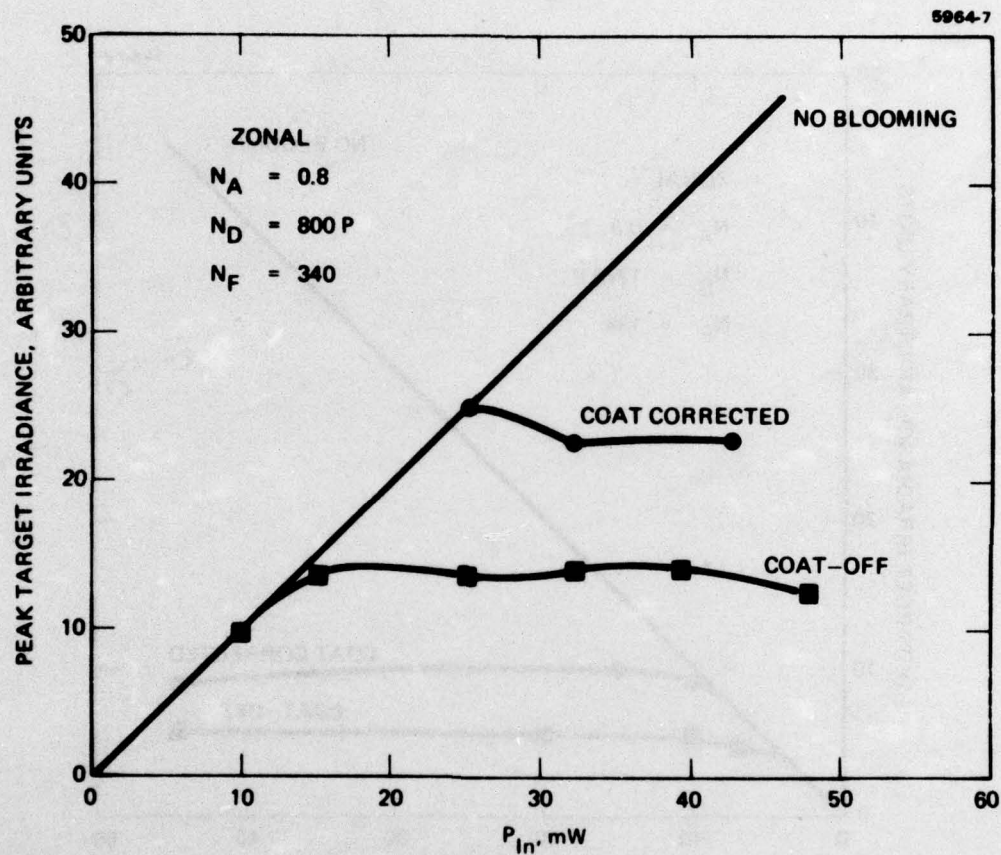


Figure 15. Peak target irradiance versus input power - zonal.
 $N_A = 0.8$, $N_D = 800P$, $N_F = 340$.

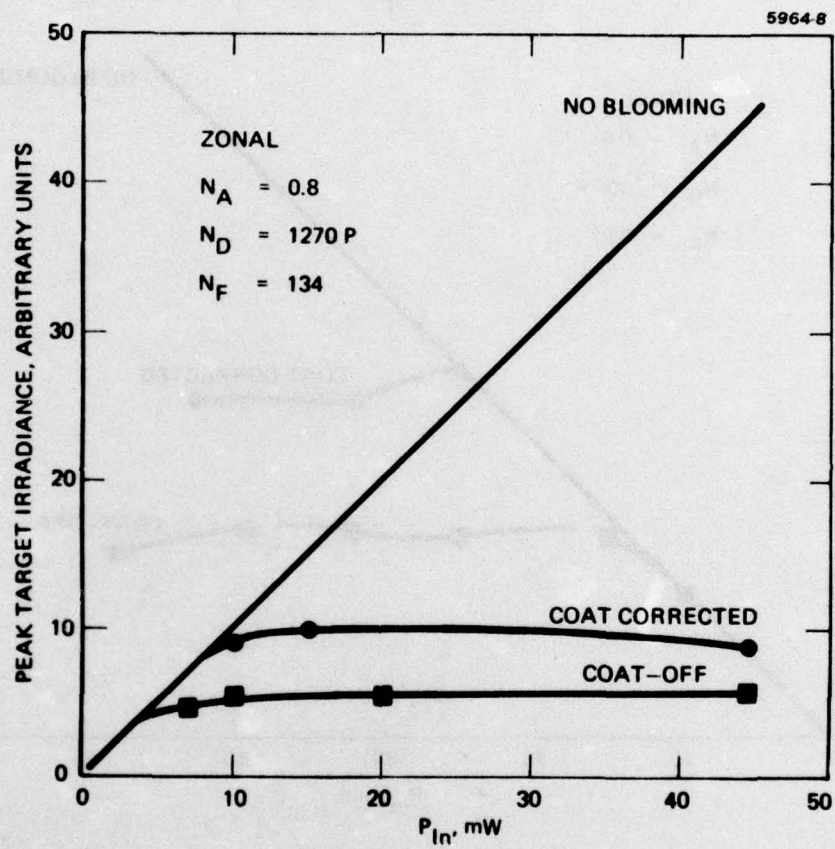


Figure 16. Peak target irradiance versus input power - zonal. $N_A = 0.8$, $N_D = 1270P$, $N_F = 134$.

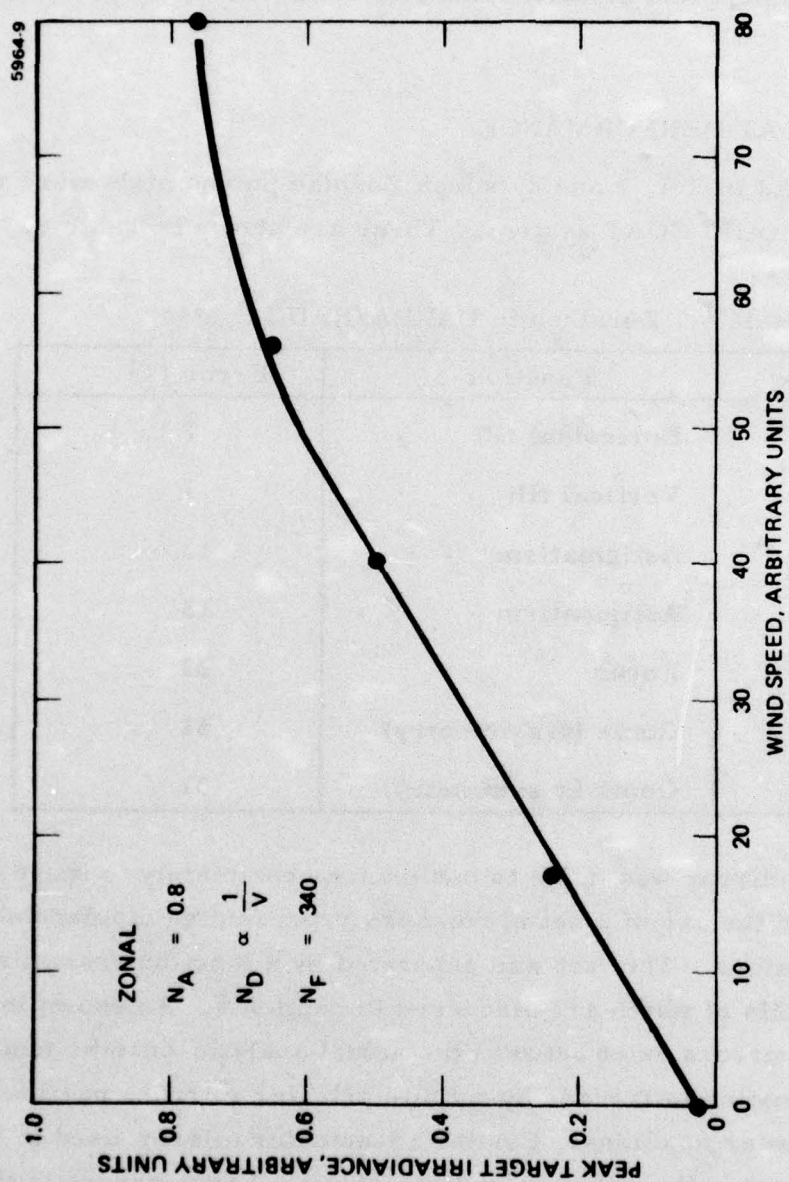


Figure 17. Peak target irradiance versus wind speed.

irradiance as a function of wind speed. Intensity increases nearly linearly over the range of the experimental conditions. This is the expected trend based on the argument that distortion number is inversely proportional to wind speed.

E. MODAL COAT PERFORMANCE

As described in Ref. 1 and 2, seven Zernike polynomials were wired into the DARPA/RADC COAT system. These are shown in Table 6.

Table 6. Zernikes in DARPA/RADC System

Zernike	Function	Error (%)
1	Horizontal tilt	7
2	Vertical tilt	7
3	Astigmatism	13
4	Astigmatism	13
5	Focus	23
6	Coma (y-symmetry)	51
7	Coma (x-symmetry)	51

The deformable mirror was made to conform approximately to these Zernike functions through the use of a set of numbers representing displacements of the various actuators. This set was generated by a function-maximization routine, the details of which are discussed in Section 4. As shown in Section 4, large errors exist between the actual analytic Zernike function and the approximation to it made by a finite actuator mirror, particularly for the higher-order functions. For the 19-actuator mirror used in the present experiments, the errors are given above. Large errors in the functions imply that they are not orthogonal and, consequently, that cross coupling would be expected to affect the results. Modal operation of the COAT system in the unbloomed (local-loop) path gave evidence of this. To investigate servo stability, each of the seven Zernikes was switched individually into the COAT system. Each one converged to a stable state.

However, when all were switched on sequentially, an unstable state resulted when the higher order Zernikes, Z6 and Z7, were included. That is, with Z1 through Z5 on, switching Z6 and/or Z7 on resulted in an unstable servo. This probably resulted from the large 50% error in the functions and the cross-coupling caused by the error. In subsequent experiments concerning blooming compensation, the results from which are discussed below, only the first 5 Zernikes listed were used.

Experiments performed for blooming compensation used three sets of the parameters N_A , N_D , and N_F . The results of these experiments are shown in Figures 18, 19, and 20. These show that in only one case (for $N_A = 0.2$, $N_D = 318$ P, and $N_F = 134$, as shown in Figure 18) did modal COAT using the 5 Zernikes give a correction. Comparing this result to the corresponding zonal case (Figure 12) indicates a reasonably similar result although the correction is somewhat poorer. However, the Zernike mode gives no apparent correction for the other cases. Again, using the auxiliary focus and tracking servos yielded the same result as had the zonal case.

It is important, when comparing the zonal and modal cases, that the local loop beam profile be the same in each case. This is so because it is this beam that is propagated into the blooming cell. Strehl-ratio measurements of the local loop beam in the modal mode gave virtually the same result as those in the zonal mode. Comparing the results of Figure 12 with those of Figure 18 shows that the COAT OFF results are slightly better in the modal mode. Comparing Figure 17 with Figure 19 and Figure 16 with Figure 20 shows that the modal COAT OFF result is nearly the same as the zonal corrected result. This implies that the near-field beam input to the cell may be different. One would expect that the corrections would be better if the blooming were not as severe. Unfortunately, this was not borne out by the results. This may have been because of the nonorthogonality of the Zernikes or because higher order Zernikes would have been needed to give a correction. Earlier analytic work on the contract showed, basically, that seven select Zernikes were necessary to give good correction in a moderate thermal blooming case. These are horizontal tilt, focus, astigmatism ($x^2 - y^2$ only), coma (y-symmetry only), spherical aberration, 5th order coma, and 5th order spherical aberration. Thus, for the present

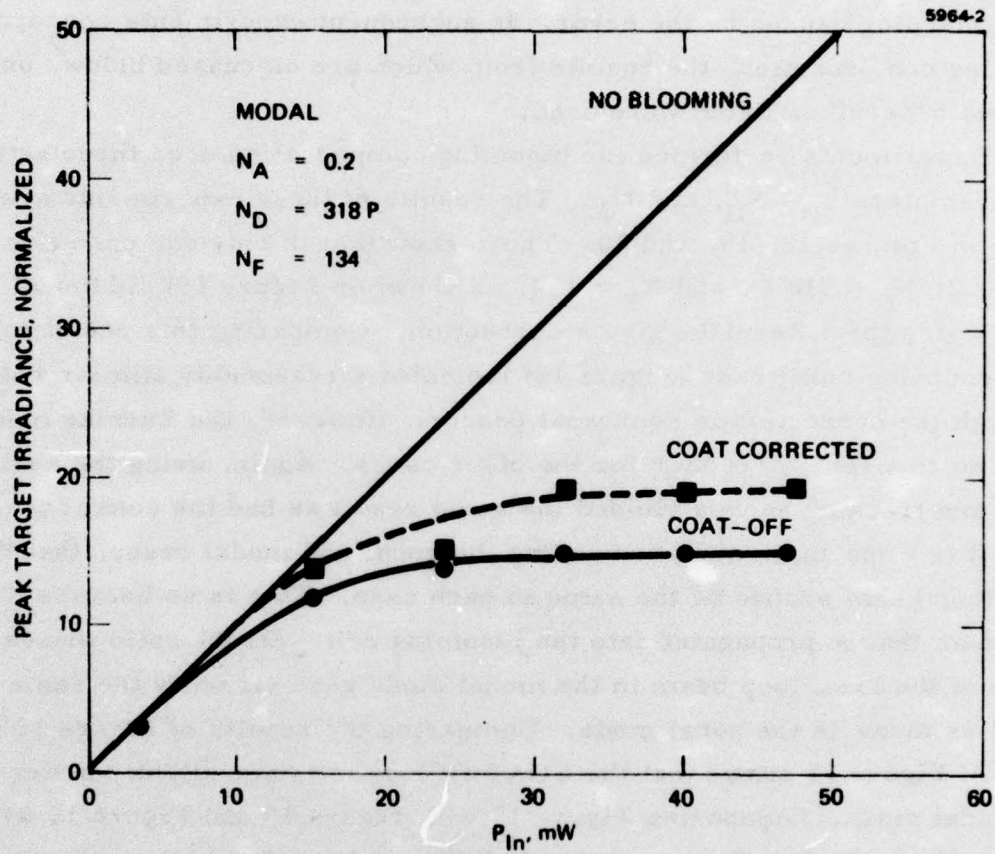


Figure 18. Peak target irradiance versus input power — model
 $N_A = 0.2$, $N_D = 318P$, $N_F = 134$.

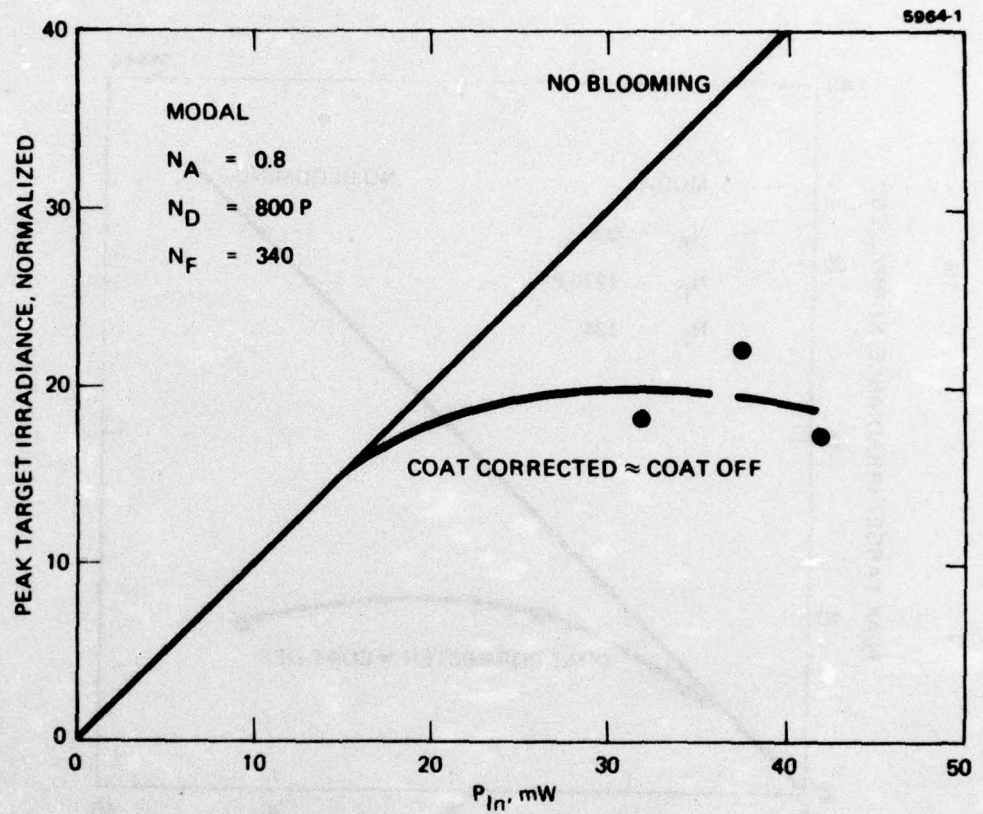


Figure 19. Peak target irradiance versus input power — model $N_A = 0.8$, $N_D = 800P$, $N_D = 340$.

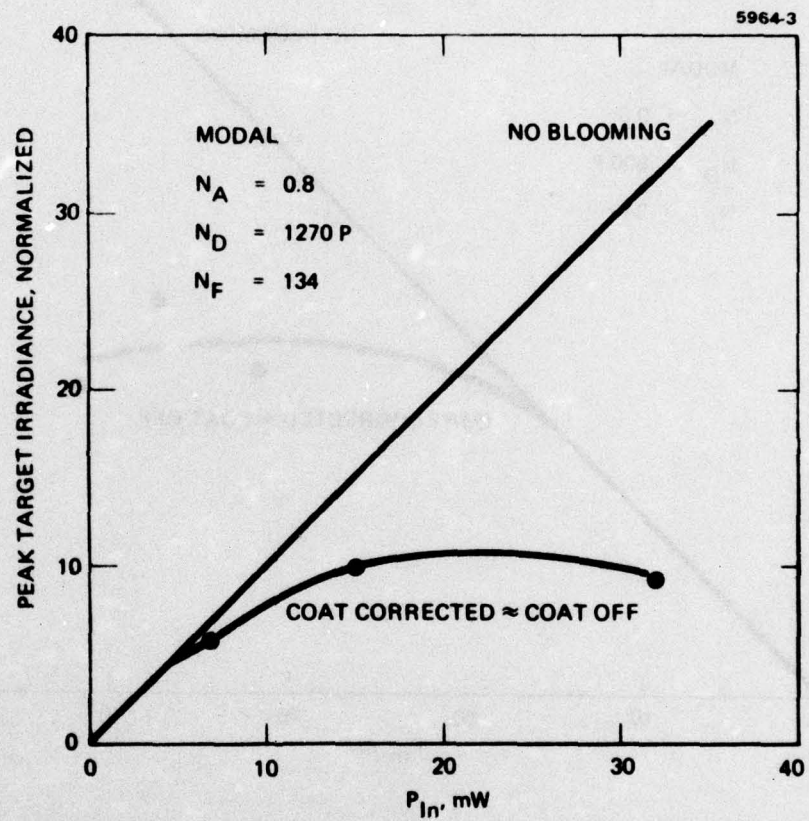


Figure 20. Peak target irradiance versus input power — model $N_A = 0.8$, $N_D = 1270P$, $N_F = 134$.

experimental measurements, only horizontal tilt, focus, and coma are effective. The remaining four functions are higher order and would require more actuators than the present 19.

Returning to the case where correction was achieved, a sequencing set of experiments with the five Zernikes was performed. The tabulated data for one power level for various combinations of Zernikes is shown in Table 7. Although other cases were run, these results are typical. Power was 0.42 (run 1) with all five on. Power dropped to 0.32 when Z5 was turned off for run 2. Power dropped to 0.34 when Z4 was turned off for run 3. No power change was observed for runs 4, 5, and 6. Runs 4, 5, and 6 correspond to astigmatism (x, y), y tilt, and x tilt. With all off (run 7), power was 0.24. These results are consistent with the analytic results from Ref. 4 discussed above and with the computer simulation work

Table 7. Zernike Sequencing

Run	Sequence	Peak Irradiance (arb.units)
1	all-on	0.42
2	4321	0.32
3	5321	0.34
4	5421	0.41
5	5431	0.42
6	5432	0.42
7	all off	0.24
8	54321	0.42
9	34512	0.42
10	other	0.42

discussed in Section 2. That is, focus and astigmatism ($x^2 - y^2$) are the most important functions in compensating for blooming. The fact that tilt was not found to be important was a result of the measurement technique (described previously). That is, since the pinhole detector was always translated to the point of maximum intensity, tilt could not affect measured peak intensity.

Runs 8, 9, and 10 represent sequences in which the 5 Zernikes were turned on. No difference in peak irradiance was obtained for any sequence (run 10 represents a large number of other sequences). What we did observe was that, regardless of when Z4 and Z5 were turned on in the sequence, the final result was always the same.

SECTION 4

ZERNIKE-POLYNOMIAL/DEFORMABLE-MIRROR APPROXIMATION

The Zernike polynomials and the calculation procedure used to generate the actuator inputs (which were required to make the deformable mirror approximate those polynomials) are described in this section. This set of actuator inputs was implemented in the DARPA/RADC deformable mirror, as discussed in Section 3.

A. ZERNIKE POLYNOMIALS

The Zernike polynomials are a complete set of orthogonal functions defined on the unit circle. A useful table of the Zernike polynomials in polar form is given in the Perkin-Elmer report RADC-TR-76-116. The first 14 of these functions and their equivalents in rectangular coordinates are reproduced in Table 8. The seven implemented in the DARPA/RADC electronics (as described in Section 3) were Z1 through Z7.

B. PROBLEM DEFINITION

A deformable mirror is typically a thin, flat, optically polished plate supported on the back by an array of extensible actuators. The actuators are attached to a massive, rigid baseplate. The actuators are usually cylinders or disc stacks of piezoelectric ceramic which can be controlled electrically to produce the desired extensions and thus to deform the mirror plate in a controlled manner. The total travel of an actuator is limited to a few wavelengths of the laser radiation so the deformation of the plate remains within the elastic limit, and the linear theory of plates is applicable.

Table 8. Zernike Polynomials

Zernike	Polar Constant	Rectangular
1	$2 r \cos \theta$	$2 x$
2	$2 r \sin \theta$	$2 y$
3	$\sqrt{6} r^2 \sin 2\theta$	$2 - 6 xy$
4	$\sqrt{6} r^2 \cos 2\theta$	$\sqrt{6} (x^2 - y^2)$
5	$\sqrt{3} (2r^2 - 1)$ defocus (longitudinal)	$\sqrt{3} (2(x^2 + y^2) - 1)$
6	$\sqrt{8} (3r^3 - 2r) \sin \theta$	$\sqrt{8} y (3(x^2 + y^2) - 2)$
7	$\sqrt{8} (3r^3 - 2r) \cos \theta$	$\sqrt{8} x (3(x^2 + y^2) - 2)$
8	$\sqrt{8} r^3 \sin 3\theta$	$\sqrt{8} y (3x^2 - y^2)$
9	$\sqrt{8} r^3 \cos 3\theta$	$\sqrt{8} x (x^2 - 3y^2)$
10	$\sqrt{5} (6r^4 - 6r^2 + 1)$ 3rd order spher.	$\sqrt{5} (6(x^2 + y^2)^2 - 6(x^2 + y^2) + 1)$
11	$\sqrt{10} (4r^4 - 3r^2) \cos 2\theta$	$\sqrt{10} (x^2 - y^2) (4(x^2 + y^2) - 3)$
12	$\sqrt{10} (4r^4 - 3r^2) \sin 2\theta$	$2\sqrt{10} xy(4(x^2 + y^2) - 3)$
13	$\sqrt{10} r^4 \cos 4\theta$	$\sqrt{10} ((x^2 + y^2)^2 - 8x^2y^2)$
14	$\sqrt{10} r^4 \sin 4\theta$	$4\sqrt{10} xy(x^2 - y^2)$

In a linear system, the principle of superposition states that the plate deformation produced by all the actuators operating together can be expressed as the algebraic summation of the deformations produced by the individual actuators acting separately. For each actuator, a unit profile can be defined. It is the profile produced on the mirror when that actuator receives unit electrical input and all other actuators receive zero input. The total profile can then be calculated as the point-by-point summation over the surface of all the unit profiles, each multiplied by the algebraic value of its electrical input at that instant.

In a real mirror, the various unit profiles will not be identical because of distortion produced by proximity to the edge of the mirror. In this study, these distortions will be neglected and it is assumed that all actuators will be characterized by identical unit profiles.

Laboratory measurements made on several mirrors³ show that the unit profiles can be characterized with good accuracy by a modified "gaussian" having circular symmetry and defined as:

$$Z = \exp (A r^n) .$$

The true gaussian corresponds to a value of $n = 2$, while the measured profiles ranged from $n = 1.5$ to $n = 2.5$. The sign of A is negative and its numerical value determines the "width" of the unit profile and hence the degree of cross coupling between adjacent actuators. This cross coupling is defined as the motion produced at the center of a given actuator when an adjacent actuator is driven with unit input. The measured values have ranged from 3 to 20%. In particular, for the DARPA/RADC mirror, $A = -5.369$ and $n = 1.71$ and the measured cross coupling was 14%.

C. SELECTED PARAMETER VALUES

For this study, the actuator array consisted of 37 actuators arranged in a "circular-hex" pattern (as shown in Figure 21). In addition, a 19-actuator study was made. This was done by not using the outer ring of actuators shown in Figure 21. The results from this 19-actuator study were implemented into the DARPA/RADC mirror. However, to facilitate an understanding of the computational scheme, the 37-actuator system will be described in detail with the 19 actuator results summarized briefly.

The unit circle of the Zernike functions passes through the centers of the outer circle of actuators. Also shown in Figure 21 is the array of mesh points on which the numerical calculations are performed. The mesh points also include a point at the center of each actuator. The total number of mesh points is 127. The expression for the unit profile for the 37-actuator study, which was chosen as a true gaussian having a coupling of 12% to adjacent actuators, is

$$z = \exp(-9.0824 r^2),$$

where r is measured from the center of the given actuator and the scale was chosen so that the unit circle has a radius of 1.

D. COMPUTER PROGRAM

The goal of the calculation was to find a vector of actuator inputs such that the form of the mirror would be optimally matched to the form of a given Zernike polynomial in the least-squares sense. Several methods were tried which failed because of poor accuracy or excessive CPU time. These included multivariate optimization (hill climbing) techniques, simulation of a complete COAT system matching a phase front in the form of a Zernike polynomial, and a method of local minimization which reduced the error in the neighborhood of each actuator. The last method gave good results but was not a true least-squares solution.

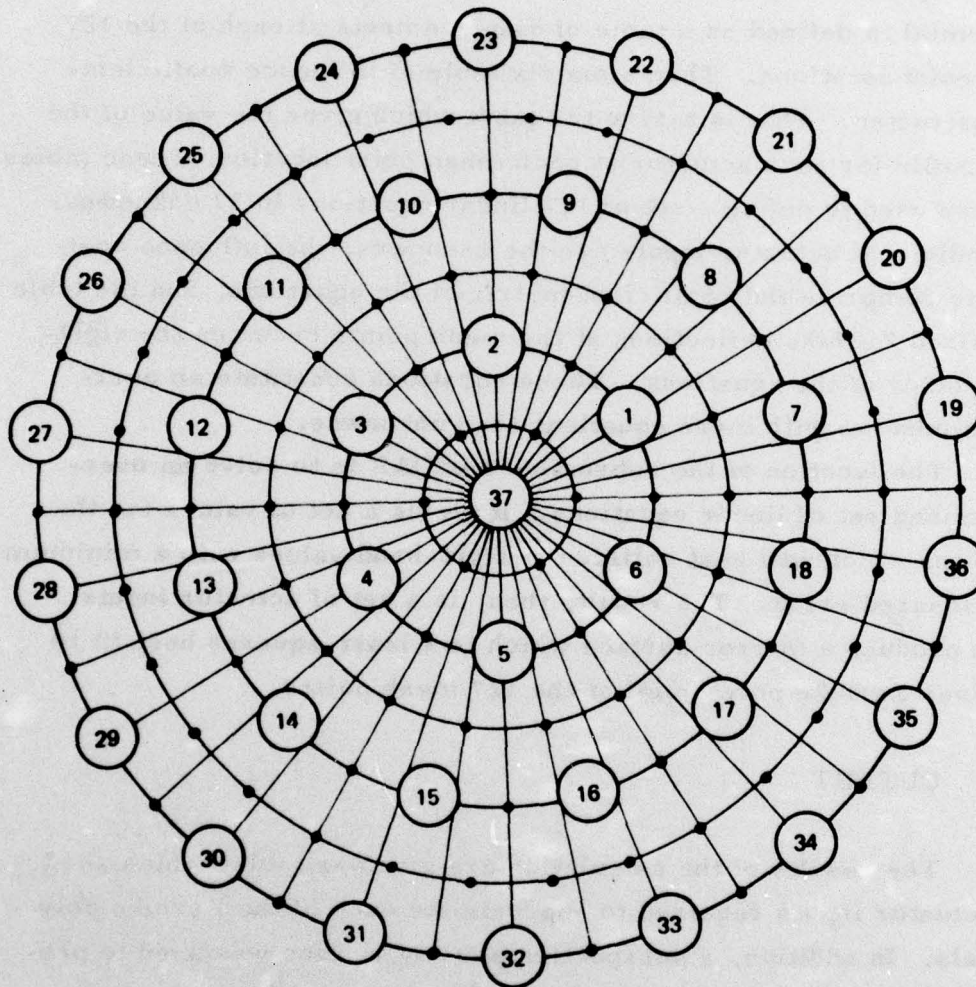


Figure 21. Actuator array pattern.

The method which was finally adopted involved application of a computer library routine called LLSQAR. The main program starts by generating a table of actuator locations and a table of mesh point locations, both in x, y coordinates. Next, the desired Zernike polynomial is defined as a table of displacements at each of the 127 mesh point locations. Then a matrix table of influence coefficients is constructed. This is a 37 x 127 table which gives the value of the unit profile for each actuator at each mesh point location. These tables are then used to define a set of 127 linear equations in 37 unknowns. The individual actuator inputs are the unknowns, the influence coefficients comprise the coefficient matrix of the equations, and the table of desired Zernike deflections at the mesh points becomes the right-hand vector of the equations. These equations constitute an over-determined set with more equations than unknowns.

The function of the subroutine LLSQAR is to solve an over-determined set of linear equations. It yields a set of values for the unknowns which will best satisfy the right-hand values with a minimum total squared error. The result, then, is a set of actuator inputs which produce a mirror surface which is a least-squares best fit to the given Zernike polynomial at the 127 mesh points.

E. OUTPUT

The results of the calculation are given as tables which show the actuator inputs required to approximate each of the Zernike polynomials. In addition, a perspective plotting routine was used to produce 3-D displays of each Zernike function, of the corresponding mirror profile, and of the error (which is the difference between the profile and the Zernike function). For each of these displays, the data is recomputed on a 41 x 41 square matrix with all points outside the unit circle being set to zero. Finally, the rms error of the approximation is computed and printed. This number is derived from the

41 x 41 error matrix and is computed as the square root of the mean squared value in this matrix, again disregarding those points outside the unit circle. The matrix contains $41 \times 41 = 1681$ points of which 1245 lie within the unit circle.

Each Zernike polynomial is normalized so that its mean square value is unity, which means that the computed errors can be read directly as per unit values. These values are shown on the corresponding displays.

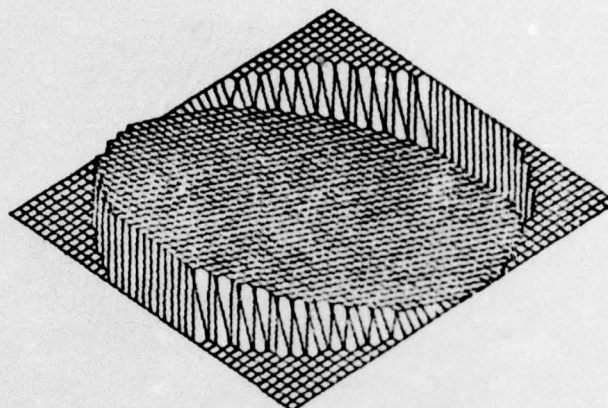
A typical result for the actuator inputs for the 37-actuator case for the focus Zernike is given in Table 9. Representative perspective plots for the tilt, focus, and coma Zernike functions are shown in Figures 22, 23, and 24, respectively. We see that, in general, generating higher order functions with the mirrors produces larger errors.

In Table 10, the rms errors for the 37 actuators and the 19-actuator mirror are given for all 14 Zernike functions. It is apparent from the errors shown in this table that, to generate higher order functions accurately, requires more actuators.

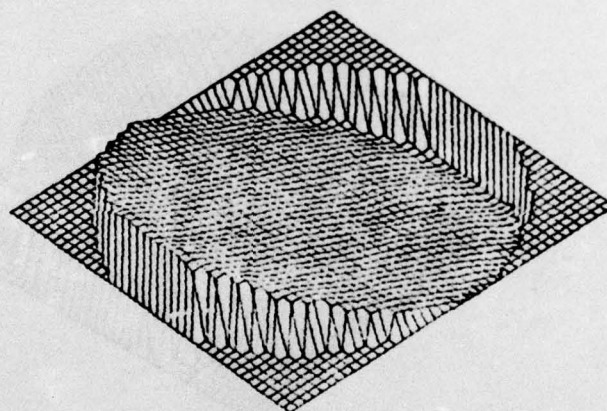
Table 9. Focus Zernike - 37 Actuators

1,	-0.9454534	.
2,	-0.9454531	.
3,	-0.9454532	.
4,	-0.9454530	.
5,	-0.9454531	.
6,	-0.9454530	.
7,	-0.3925271	.
8,	-0.3925270	.
9,	-0.3925270	.
10,	-0.3925271	.
11,	-0.3925272	.
12,	-0.3925270	.
13,	-0.3925274	.
14,	-0.3925273	.
15,	-0.3925271	.
16,	-0.3925270	.
17,	-0.3925274	.
18,	-0.3925274	.
19,	1.452072	.
20,	1.453899	.
21,	1.452072	.
22,	1.452072	.
23,	1.453898	.
24,	1.452072	.
25,	1.452072	.
26,	1.453898	.
27,	1.452072	.
28,	1.452072	.
29,	1.453898	.
30,	1.452072	.
31,	1.452072	.
32,	1.453899	.
33,	1.452072	.
34,	1.452072	.
35,	1.453898	.
36,	1.452072	.
37,	-1.072329	.
RMS ERROR = 0.1314		

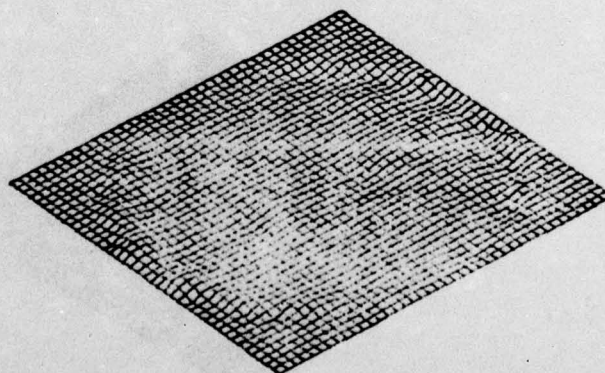
ONLY COPY AVAILABLE



(a) ZERNIKE

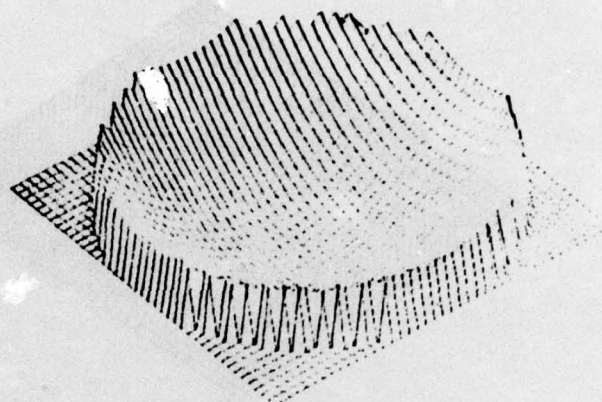


(b) MIRROR

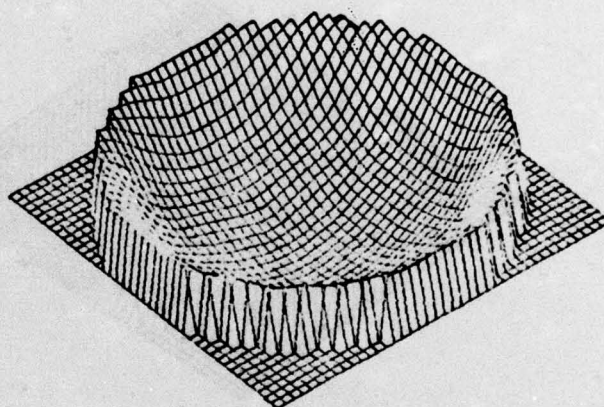


(c) ERROR rms = 5.2%

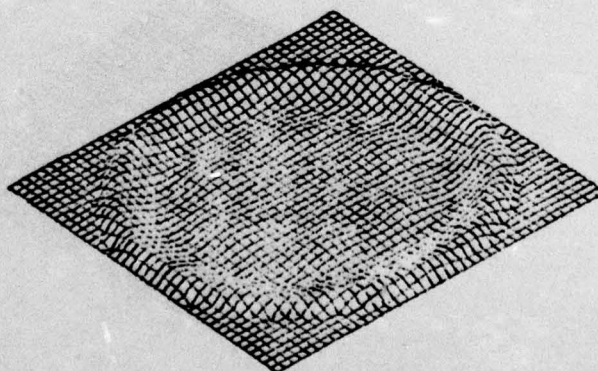
Figure 22. Tilt Zernike junction.



(a) ZERNIKE

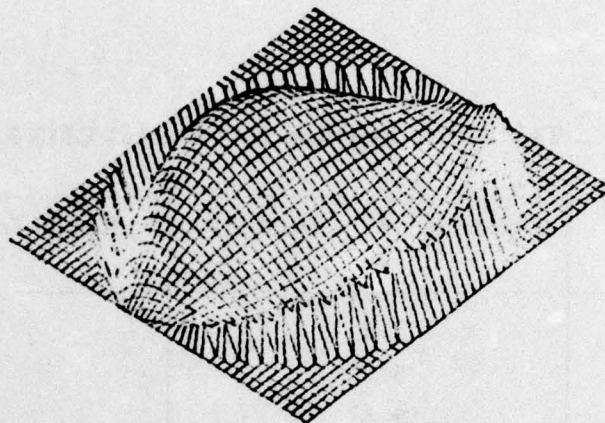


(b) MIRROR

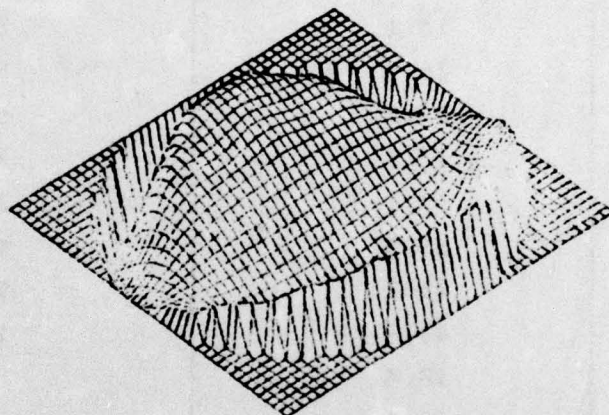


(c) ERROR rms = 13.1%

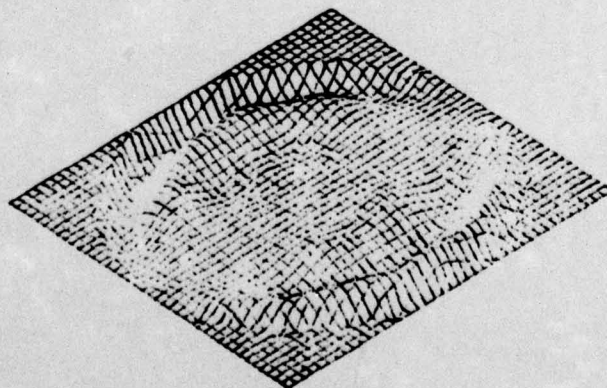
Figure 23. Focus Zernike function.



(a) ZERNIKE



(b) MIRROR



(c) ERROR rms = 26.7%

Figure 24. Coma Zernike junction.

Table 10. Zernike Polynomial RMS Errors

Zernike	Error for 37 Actuators, %	Error for 19 Actuators, %
1	5.2	6.6
2	5.2	6.6
3	8.5	12.8
4	8.5	12.8
5	13.1	22.7
6	26.7	50.7
7	26.7	50.7
8	12.7	21.9
9	12.7	21.9
10	55.3	95.2
11	43.3	78.8
12	43.3	78.8
13	18.4	-
14	18.4	-

SECTION 5

RECOMMENDATIONS FOR FUTURE WORK

Although the experimental and analytic results obtained from this work indicate definite trends as to what algorithms can be used for blooming compensation, the results have also indicated several areas for further investigation. In particular, to achieve a more conclusive comparison between the zonal and the modal systems using Zernike polynomials will require more actuators in the deformable mirror. This would permit higher-order Zernikes to be used and prevent a large degree of cross coupling for those used. In addition, it would be desirable to have a mirror with a more consistent surface excursion from actuator to actuator (see the third interim report). This would require time-consuming polishing of the PZT stacks for each actuator.

The additional capabilities of slewing the beam would be a natural extension of the blooming scenarios studied under the contract. For the numerical studies, the most important extension is to perform the same type of study using the more costly 2-D routines just made operational at Hughes. With such results, a detailed quantitative comparison of theory and experiment could be made.

REFERENCES

1. J. E. Perason, K. M. Brown, P. G. Finucane, M. L. Minden, K. D. Price, and C. W. Yeh, "Multidither Adaptive Algorithms," Interim Report 1, December 1975.
2. J. E. Pearson, S. Hansen, M. L. Minden, and C. Yeh, "Multidither Adaptive Algorithms," Interim Report 2, September 1976.
3. R. C. Lind, K. D. Price, K. M. Brown, T. Calderone, J. E. Pearson, S. Hansen, T. A. Nussmeier, and F. J. McClung, "Multidither Adaptive Algorithms," Interim Report 3, January 1977.
4. J. E. Pearson, W. P. Brown, Jr., S. A. Kokorowski, M. E. Pedinoff, and C. Yeh, "COAT Measurements and Analysis," Final Report, January 1976.
5. L. C. Bradley and J. Herrmann, J. Opt. Soc. Am. 61, 668 (1971).

PRECEDING PAGE BLANK NOT FILMED

METRIC SYSTEM

BASE UNITS:

Quantity	Unit	SI Symbol	Formula
length	metre	m	...
mass	kilogram	kg	...
time	second	s	...
electric current	ampere	A	...
thermodynamic temperature	kelvin	K	...
amount of substance	mole	mol	...
luminous intensity	candela	cd	...

SUPPLEMENTARY UNITS:

plane angle	radian	rad	...
solid angle	steradian	sr	...

DERIVED UNITS:

Acceleration	metre per second squared	...	m/s
activity (of a radioactive source)	disintegration per second	...	(disintegration)/s
angular acceleration	radian per second squared	...	rad/s
angular velocity	radian per second	...	rad/s
area	square metre	...	m
density	kilogram per cubic metre	...	kg/m
electric capacitance	farad	F	A·s/V
electrical conductance	siemens	S	A/V
electric field strength	volt per metre	...	V/m
electric inductance	henry	H	V·s/A
electric potential difference	volt	V	W/A
electric resistance	ohm	...	V/A
electromotive force	volt	V	W/A
energy	joule	J	N·m
entropy	joule per kelvin	...	J/K
force	newton	N	kg·m/s
frequency	hertz	Hz	(cycle)/s
illuminance	lux	lx	lm/m
luminance	candela per square metre	...	cd/m
luminous flux	lumen	lm	cd·sr
magnetic field strength	ampere per metre	...	A/m
magnetic flux	weber	Wb	V·s
magnetic flux density	tesla	T	Wb/m
magnetomotive force	ampere	A	...
power	watt	W	J/s
pressure	pascal	Pa	N/m
quantity of electricity	coulomb	C	A·s
quantity of heat	joule	J	N·m
radiant intensity	watt per steradian	...	W/sr
specific heat	joule per kilogram-kelvin	...	J/kg·K
stress	pascal	Pa	N/m
thermal conductivity	watt per metre-kelvin	...	W/m·K
velocity	metre per second	...	m/s
viscosity, dynamic	pascal-second	...	Pa·s
viscosity, kinematic	square metre per second	...	m/s
voltage	volt	V	W/A
volume	cubic metre	...	m
wavenumber	reciprocal metre	...	(wave)/m
work	joule	J	N·m

SI PREFIXES:

Multiplication Factors	Prefix	SI Symbol
1 000 000 000 000 = 10 ¹²	tera	T
1 000 000 000 = 10 ⁹	giga	G
1 000 000 = 10 ⁶	mega	M
1 000 = 10 ³	kilo	k
100 = 10 ²	hecto*	h
10 = 10 ¹	deka*	da
0.1 = 10 ⁻¹	deci*	d
0.01 = 10 ⁻²	centi*	c
0.001 = 10 ⁻³	milli	m
0.000 001 = 10 ⁻⁶	micro	μ
0.000 000 001 = 10 ⁻⁹	nano	n
0.000 000 000 001 = 10 ⁻¹²	pico	p
0.000 000 000 000 001 = 10 ⁻¹⁵	femto	f
0.000 000 000 000 000 001 = 10 ⁻¹⁸	atto	a

* To be avoided where possible.